A Global Ocean-Atmosphere Climate Model. Part I. The Atmospheric Circulation

SYUKURO MANABE, KIRK BRYAN AND MICHAEL J. SPELMAN

Geophysical Fluid Dynamics Laboratory/NOAA, Princeton University, Princeton, N. J. 08540

(Manuscript received 8 February 1974, in revised form 28 June 1974)

ABSTRACT

A joint ocean-atmosphere model covering the entire globe has been constructed at the Geophysical Fluid Dynamics Laboratory (GFDL) of NOAA. This model differs from the earlier version of the joint model of Bryan and Manabe both in global domain and inclusion of realistic rather than idealized topography. This part of the paper describes the structure of the atmospheric portion of the joint model and discusses the atmospheric circulation and climate that emerges from the time integration of the model. The details of the oceanic part are given by Bryan *et al.* (1974), hereafter referred to as Part II.

The atmospheric part of the model incorporates the primitive equations of motion in a spherical coordinate system. The numerical problems associated with the treatment of mountains are minimized by using the "sigma" coordinate system in which pressure, normalized by surface pressure, is the vertical coordinate. For vertical finite differencing, nine levels are chosen so as to represent the planetary boundary layer and the stratosphere as well as the troposphere. For horizontal finite differencing, the regular latitude-longitude grid is used. To prevent linear computational instability in the time integration, Fourier filtering is applied in the longitudinal direction to all prognostic variables in higher latitudes such that the effective grid size of the model is approximately 500 km everywhere.

For the computation of radiative transfer, the distribution of water vapor, which is determined by the prognostic system of water vapor, is used. However, the distributions of carbon dioxide, ozone and cloudiness are prescribed as a function of latitude and height and assumed to be constant with time. The temperature of the ground surface is determined such that it satisfies the condition of heat balance.

The prognostic system of water vapor includes the contribution of three-dimensional advection of water vapor and condensation in case of supersaturation. To simulate moist convection, a highly idealized procedure of moist convective adjustment is introduced. The prediction of soil moisture and snow depth is based upon the budget of water, snow and heat. Snow cover and sea ice are assumed to have much larger albedos than soil surface or open sea, and have a very significant effect upon the heat balance of the surface of the model.

Starting from the initial conditions of an isothermal and dry atmosphere at rest, the long-term integration of the joint model is conducted with the economical method adopted by Bryan and Manabe in their earlier study. The climate that emerges from this integration includes some of the basic features of the actual climate. However, it has many unrealistic features, which underscores the necessity of further increasing the computational resolution of horizontal finite differencing.

In order to identify the effect of the ocean currents upon climate, the joint model climate is compared with another climate obtained from the time integration of a so-called "A-model" in which oceanic regions are occupied by wet swampy surfaces without any heat capacity. Based upon the comparison between these two climates, the possible effects of oceanic heat transport on the climate are discussed. For example, the results show that the total poleward transport of energy is affected little by the oceanic heat transport. Although ocean currents significantly contribute to the transport, the atmospheric transport of energy in the presence of the latter decreases by approximately the same magnitude. Therefore, the total transport in the joint model differs little from that in the A-model. Further comparison between the two models indicates that ocean currents significantly affect not only the horizontal distribution of surface temperature of both oceans and continents but also the global distribution of precipitation.

1. Introduction

The goal of the present study is to construct a joint ocean-atmosphere model which is capable of simulating the basic features of the climate. As we know, the interaction between the ocean and the atmosphere is one of the most important processes which control the climate. Using the joint model, one can perform controlled numerical experiments designed to identify the roles of ocean currents in maintaining the climate.

Recently, Bryan and Manabe (Bryan, 1969; Manabe, 1969b; Manabe and Bryan, 1969) constructed a joint ocean-atmosphere model with limited computational domain (one-third of the globe) and highly idealized topography. Despite many simplifications adopted for

the construction of the model, their study seems to demonstrate the feasibility of obtaining a quasi-equilibrium climate[1] with many realistic features from the numerical time integration of a joint model. Encouraged by these results, we decided to construct a joint model with global computational domain and with realistic topography. This paper describes the basic structure of the preliminary version of the global ocean-atmosphere model, and discusses some of the results from the numerical experiments.

As mentioned above, one of the major objectives of this study is to identify the effects of ocean currents in maintaining the climate. The basic strategy of this study is essentially similar to the one adopted by Bryan and Manabe. In order to determine the effects of ocean currents, two numerical experiments are performed. The first experiment is carried out by use of the joint ocean-atmosphere model, and a so-called "A-model" is used for the second experiment. In the A-model, oceans are replaced by a wet swampy surface without any heat capacity. The swamp of the A-model resembles the actual ocean with respect to the availability of moisture but differs because it lacks the effect of horizontal heat transport. By comparing the two climates which emerge from these numerical experiments, we expect to identify the effects of ocean currents upon the climate.

For the sake of economy in the computation, the numerical time integrations of both the joint model and the A-model are divided into two stages. During the first stage, the models with coarse computational resolution (grid size $\sim$500 km) are used. The integration is performed long enough for the models to nearly reach the state of quasi-equilibrium. The second stage of integration follows the first stage after doubling the computational resolution of the models. This study deals only with the first stage, coarse resolution models. As Manabe *et al.* (1970) and Holloway and Manabe (1971) have pointed out, the results from the GFDL models improve markedly when the grid size is reduced from 500 to 250 km. Accordingly, the present results suffer greatly from the coarseness of computational resolution, and do not represent the potential performance of the present-generation general circulation models. Nevertheless, these results yield useful insight about the effects of the ocean circulation upon climate and also demonstrate the feasibility of constructing a joint model capable of reproducing the realistic climate.

2. Description of the model

The atmospheric model described here is not very different from the model constructed by Holloway and Manabe (1971). However, the finite-difference computation is performed on the regular latitude-longitude grid instead of the irregular grid adopted for their study.

[1] Here, quasi-equilibrium climate implies a quasi-steady state of the model atmosphere in which state variables fluctuate around certain constant values.

The treatment of the interaction between the ocean and the atmosphere is essentially similar to the method adopted by Bryan (1969) and Manabe (1969b).

a. Model equations

In deriving the equations of motion, we adopted the "σ-coordinate" system in which the pressure, normalized by surface pressure, is chosen as the vertical coordinate (Phillips, 1957). Making the hydrostatic assumption, we may write the momentum equations on a spherical surface as

$$\frac{\partial}{\partial t}(p_* u) = -D_3(u) + \left(f + \frac{\tan\theta}{a} u\right) p_* v - p_* \left(\frac{\partial \phi}{a \cos\theta \partial \lambda}\right)_p + {}_H F_\lambda + {}_v F_\lambda, \quad (1)$$

$$\frac{\partial}{\partial t}(p_* v) = -D_3(v) - \left(f + \frac{\tan\theta}{a} u\right) p_* u - p_* \left(\frac{\partial \phi}{a \partial \theta}\right)_p + {}_H F_\theta + {}_v F_\theta, \quad (2)$$

where u and v are the eastward and northward components of the wind, respectively; p_* the surface pressure; ϕ the geopotential height; θ, latitude; λ, longitude; a the radius of the earth; f the Coriolis parameter; and ${}_H F$, ${}_v F$ are the frictional forces due to subgrid-scale mixing in the horizontal and vertical directions, respectively (see Section 2e for details of these frictional terms). The subscript p attached to the pressure gradient terms indicates differentiation on an isobaric rather than a σ-surface. This formulation of pressure gradient terms is chosen such that it reduces the inaccuracy involved in the numerical computation. For further discussion of this subject, see Holloway and Manabe (1971). The three-dimensional divergence operator $D_3(\ )$ is defined by

$$D_3(\ ) = D_2(\ ) + \frac{\partial [(\ ) p_* \dot{\sigma}]}{\partial \sigma}, \quad (3)$$

where σ denotes the individual change of normalized pressure σ, and

$$D_2(\ ) = \frac{\partial [(\ ) p_* u]}{a \cos\theta \partial \lambda} + \frac{\partial [(\ ) p_* v \cos\theta]}{a \cos\theta \partial \theta}. \quad (4)$$

The continuity equation may be written as

$$\frac{\partial p_*}{\partial t} = -D_3(1). \quad (5)$$

Integration of (5) with respect to σ yields the following equation which is used for the prediction of surface

pressure:

$$\frac{\partial p_*}{\partial t}=-\int_0^1 D_2(1)d\sigma. \tag{6}$$

The vertical σ- and p-velocities can be obtained from the following diagnostic relations, which are obtained by integrating (5) again with respect to σ:

$$\sigma=p_*^{-1}\left[-\sigma\frac{\partial p_*}{\partial t}-\int_0^\sigma D_2(1)d\sigma\right], \tag{7}$$

$$\omega=p_*\dot{\sigma}+\sigma\left[\frac{\partial p_*}{\partial t}+u\frac{\partial p_*}{a\cos\theta\partial\lambda}+v\frac{\partial p_*}{a\partial\theta}\right], \tag{8a}$$

$$=p_*\dot{\sigma}+\sigma\left[\frac{\partial p_*}{\partial t}+D_2(1)-p_*\left(\frac{\partial u}{a\cos\theta\partial\lambda}+\frac{\partial(v\cos\theta)}{a\cos\theta\,\partial\theta}\right)\right]. \tag{8b}$$

The vertical p-velocity, ω, is necessary for computing the adiabatic heating (or cooling) term in the thermodynamic equation (10) described below. We found that the finite-difference representation of (8a) caused serious computational difficulties in areas of irregular topography. Therefore, the form (8b) is used for the actual computation.

The geopotential height can be obtained by integrating the following hydrostatic equation with respect to σ:

$$\frac{\partial\phi}{\partial\sigma}=-\frac{RT}{\sigma}, \tag{9}$$

where R is the gas constant of air and T is temperature, the ideal gas being assumed for the atmosphere.

The temperature tendency equation based on the thermodynamic equation is

$$\frac{\partial}{\partial t}(p_*T)=-D_3(T)+\frac{R}{c_p}\frac{T\omega}{\sigma}+(1/c_p)[p_*Q_c+p_*Q_{\mathrm{RAD}}]+{}_HF_T+{}_vF_T, \tag{10}$$

where c_p is the specific heat of air under constant pressure; Q_c and Q_{RAD} represent the heating (or cooling) by condensation or convection processes and by radiation, respectively; and ${}_HF_T$ and ${}_vF_T$ represent the contribution of the horizontal and vertical subgrid-scale mixing, respectively, and are discussed in Section 2e.

The tendency equation used for predicting mixing ratio r in the model is

$$\frac{\partial}{\partial t}(p_*r)=-D_3(r)+[p_*C]+{}_HF_r+{}_vF_r, \tag{11}$$

where C denotes large-scale condensation and moist convection processes; and ${}_HF_r$ and ${}_vF_r$ represent the contributions of the horizontal subgrid-scale mixing and vertical subgrid-scale mixing due to forced convection, respectively. They are described in Section 2e.

b. Finite-difference formulation

1) FINITE-DIFFERENCE OPERATORS

The system of finite-difference equations of this model is obtained by modifying the formulation of Kurihara and Holloway (1967). It is based upon the concept of the "box method" proposed by Bryan (1966) and is essentially similar to the energy-conserving system suggested earlier by Lilly (see Smagorinsky *et al.*, 1965).

The finite-difference form of flux divergence operators $D_2(\ )$ and $D_3(\ )$ appearing in the system of equations of Section 2a are given by

$$D_2(\ )\Leftarrow\frac{\delta_\lambda[\overline{p_*u}^{\lambda}\overline{(\ )}^{\lambda}]}{a\cos\theta\cdot\Delta\lambda}+\frac{\delta_\theta[\overline{p_*v}^{\theta}\overline{(\ )}^{\theta}\cos\theta]}{a\cos\theta\cdot\Delta\theta}, \tag{12}$$

$$D_3(\ )\Leftarrow D_2(\ )+\frac{\delta_\sigma[p_*\dot{\sigma}\overline{(\ )}^{\sigma}]}{\Delta\sigma}, \tag{13}$$

where the symbol $\Leftarrow$ implies that the expression on the right side of this symbol represents the finite-difference form of the expression on the left; and where, for example,

$$\delta_\lambda\phi=\left[\phi\left(\lambda+\frac{\Delta\lambda}{2}\right)-\phi\left(\lambda-\frac{\Delta\lambda}{2}\right)\right], \tag{14}$$

$$\overline{\phi}^{\lambda}=\frac{1}{2}\left[\phi\left(\lambda+\frac{\Delta\lambda}{2}\right)+\phi\left(\lambda-\frac{\Delta\lambda}{2}\right)\right]. \tag{15}$$

In these equations, $\Delta\theta$ and $\Delta\lambda$ are latitudinal and longitudinal grid size angle, respectively; and $\Delta\sigma$ denotes the σ-thickness between two neighboring half-levels as identified in Table 1. The pressure gradient terms in finite-difference form are

$$\left(\frac{\partial\phi}{a\cos\theta\cdot\partial\lambda}\right)_p\Leftarrow\frac{(\delta_\lambda\overline{\phi}^{\lambda})_p}{a\cos\theta\cdot\Delta\lambda}, \tag{16}$$

$$\left(\frac{\partial\phi}{a\cdot\partial\theta}\right)_p=\left[\frac{\partial(\phi\cos\theta)}{a\cos\theta\cdot\partial\theta}\right]_p-\phi\left[\frac{\partial(\cos\theta)}{a\cos\theta\cdot\partial\theta}\right]_p\Leftarrow\frac{[\delta_\theta(\overline{\phi}^{\theta}\cdot\cos\theta)]_p}{\cos\theta\cdot(a\Delta\theta)}-\phi\frac{[\delta_\theta(\cos\theta)]_p}{\cos\theta\cdot(a\Delta\theta)}. \tag{17}$$

2) GLOBAL GRID SYSTEM

A part of the global grid system adopted for this model is shown in Fig. 1. Each latitude circle contains 64 grid points and each hemisphere has 19 rows of grid points between the equator and the pole. The merit of this system over the irregular grid system of Kurihara

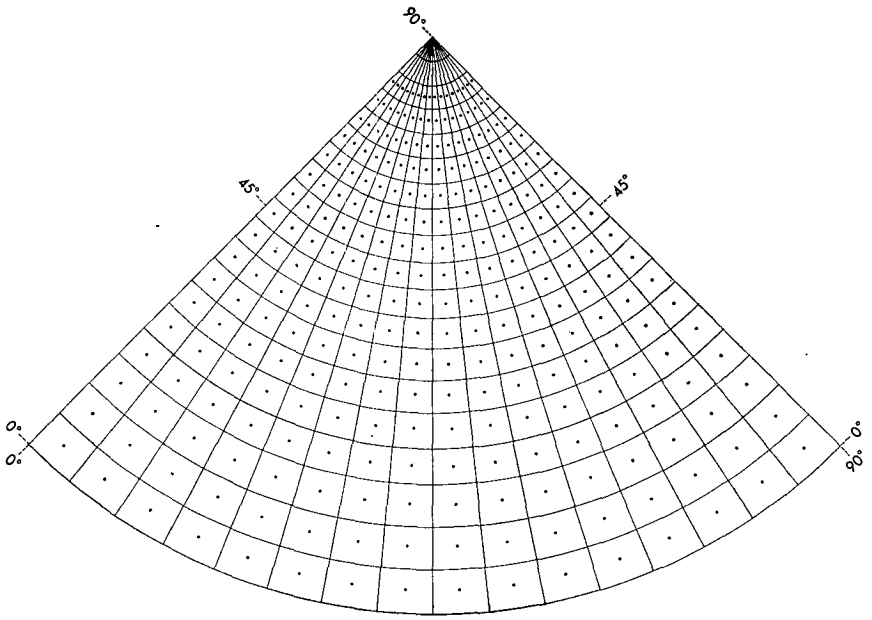

FIG. 1. One-eighth of the global computational grid, projected on a polar stereographic plane. Dots are omitted from the northern-most two rows due to lack of space.

and Holloway (1967) was discussed by Vanderman (1970), and by Holloway *et al.* (1973). As Fig. 1 indicates, grid points are spaced equally in the meridional and longitudinal directions. At the center of each box, horizontal components of the wind vector, surface pressure, temperature, and mixing ratio of water vapor are specified.

The indexing of the levels for the finite differencing in the vertical direction is illustrated in Fig. 2. At each integer level, u, v, T, r, ϕ and ω are obtained and vertical σ-velocity ($\dot{\sigma}$) is computed at each half-level. The nine model levels are spaced unevenly in the vertical from the lowest at about 80 m height up to a top level at approximately 28 km above the ground. The σ-coordinate system is used to facilitate the incorporation of mountains into the model. In this σ-system the levels are surfaces of constant ratio of pressure to surface pressure. A tabulation of the σ-levels and their approximate elevations above the surface points at sea level is shown in Table 1.

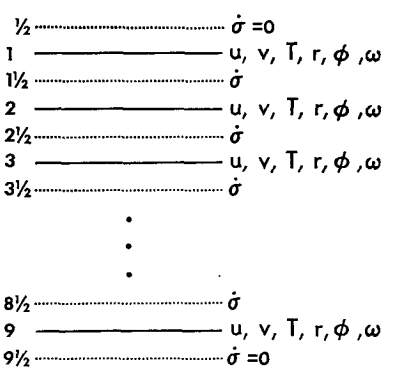

FIG. 2. The indexing scheme for the vertical finite differencing.

Fig. 3 shows the distribution of surface topography used in the model experiments. The method for deriving the smoothed topography is discussed in the Appendix.

3) TIME INTEGRATION

The numerical time integration of the model is carried out with the so-called "leap frog" method (centered differencing). The time interval chosen for this integration is 10 min. In order to avoid the development of the computational mode, the wind, temperature, humidity and pressure fields of the model atmosphere at three consecutive time steps are averaged once every 40 time steps by the weights 0.25, 0.50 and 0.25. After such a time smoothing, the integration is performed by the so-called "Euler backward" scheme proposed by Matsuno (1966) for one time step before resuming the integration by the regular leap frog method. This application of the Euler backward method is required to avoid the conventional forward time step which is computationally unstable.

4) FOURIER FILTERING

To prevent linear instability from occurring in the time integration on the latitude-longitude grid, we apply Fourier space filtering to all time-integrated variables at each time step as suggested by Holloway *et al.* (1973). Otherwise, a progressively shorter time step would have to be used as the time integration advances toward the poles, where the east-west grid-point spacing becomes

FIG. 3. Topography of the earth's surface (10^2 m) used for both the joint model and the A-model.

smaller (Grimmer and Shaw, 1967). The filtering method is applied to higher latitudes where the length of latitude circles decreases rapidly with increasing latitudes. Accordingly, it prevents the east-west wavelength of the shortest wave from getting shorter than a certain critical value. The minimum wavelength, $L_{\min}$, is specified as

$$L_{\min}=(2\pi a\cos\theta_c)/(N/2), \tag{18}$$

where θ_c is the equatorward boundary of the filtered region, and N the number of grid points in a latitude circle. For the present model, $\theta_c=45°$. In other words, $L_{\min}$ is equal to two grid distances at latitude θ_c. This minimum wavelength is guaranteed by limiting the maximum wavenumber at latitude $\theta(>\theta_c)$ to

$$k_{\max}=(2\pi a\cos\theta)/L_{\min}=\tfrac{1}{2}N(\cos\theta/\cos\theta_c). \tag{19}$$

In practice, $k_{\max}$ must be rounded to the nearest integer and $L_{\min}$ is thereby slightly altered.

The Fourier filter described above insures that the effective longitudinal grid size [i.e., $(2\pi a\cos\theta)/(2k_{\max})$] is nearly constant irrespective of latitude. Equatorward of latitude θ_c, i.e., 45°, no Fourier filter is applied because the east-west grid size varies very slowly with latitude. (Longitudinal grid size is made approximately equal to latitudinal grid size at 32° latitude.) In short, both effective longitudinal grid sizes in the filtered region and longitudinal grid sizes in the unfiltered region are not very different from the latitudinal grid size, i.e., 526 km.

The space filtering is accomplished by analyzing the data along each latitude circle into their Fourier components and resynthesizing the data with only the desired waves present. It can be shown that this filtering scheme has no significant effect on the quadratic conserving properties of finite-difference equations because the truncated components are orthogonal to the retained ones.

In the case of vector variables, we transform the components to a polar stereographic projection before

TABLE 1. The σ-levels and their approximate elevations above the surface points at sea level.

Level	$\sigma=p/p_*$	Height (m)
0.5	0.00000000	∞
1.0	0.01594441	27,900
1.5	0.04334139	21,370
2.0	0.07000000	18,330
2.5	0.11305591	15,290
3.0	0.16500000	12,890
3.5	0.24081005	10,500
4.0	0.31500000	8680
4.5	0.41204675	6860
5.0	0.50000000	5430
5.5	0.60672726	4010
6.0	0.68500000	3060
6.5	0.77337055	2110
7.0	0.83500000	1490
7.5	0.90154066	860
8.0	0.94000000	520
8.5	0.98010000	170
9.0	0.99000000	80
9.5	1.00000000	0

the Fourier filtering is performed. This is done because of the sharp variation of the unit vector of spherical coordinates around the pole.

It is necessary to apply the same Fourier filter to the surface topography at the beginning of the time integration. Failure to do so usually results in a rapid excitation of gravity waves.

c. Radiative transfer

The scheme for computing the radiative heating and cooling is identical to that described by Manabe and Strickler (1964) and Manabe and Wetherald (1967). The scheme consists of computations for longwave radiation and for solar radiation. The principles of computing the flux of longwave radiation are not very different from those adopted for constructing a so-called "radiation" diagram such as the one proposed by Yamamoto (1952). In this study, the diurnal and seasonal variation of solar radiation is eliminated by use of an effective mean zenith angle of the sun for each latitude. The gaseous absorbers (water vapor, carbon dioxide and ozone) are included for the computation of both solar and terrestrial radiation. In addition, the effects of clouds are incorporated into the scheme. For the computation of terrestrial radiation, a cloud is assumed to be a blackbody. Separate values of albedo are assigned to various categories of clouds in the computation of the fluxes of solar radiation.

The distribution of mixing ratio of water vapor, which is required for the computation of radiative transfer, is computed by the prognostic equation of water vapor [Eq. (11)]. The annual mean distribution of the concentration of ozone is determined from ozone measurements by Hering and Borden (1965) as a function of latitude and height. Their total amounts are normalized in such a way that they coincide with the distributions compiled by London (1962) who used extensive measurements of total ozone obtained by a Dobson spectrometer. The mixing ratio of carbon dioxide is assumed to have a constant value of 0.0456% by weight everywhere. Clouds are classified as high, middle, and low—the latter including cumuliform. The annual mean distribution of these clouds is determined from the table of cloud amounts compiled by London (1957).

The annual mean distribution of albedo over oceanic surfaces and over snow-free land surfaces is specified from the distribution of albedo compiled by Posey and Clapp (1964). The albedo of snow-covered surfaces is computed as a function of snow depth. Based on the results of Kung *et al.* (1964), the following formulas were derived:

$$A=A_b+(S_w)^{\frac{1}{2}}(A_s-A_b), \quad \text{if } S_w<1 \text{ cm}, \tag{20}$$

$$A=A_s, \quad \text{if } S_w\geqslant 1 \text{ cm}, \tag{21}$$

where A_b and A_s are the albedos of bare soil and of deep snow, respectively, and A is the albedo of the earth's surface covered by snow of water equivalent S_w, assumed here to be one-tenth of the snow depth. For our computations, A_s is assumed to be 0.60. When pack ice is present over the sea, an albedo of 0.35 is used. Poleward of latitude 70°, however, the albedo over snow-covered land and over pack ice is assumed to be 0.70 everywhere.

d. Convection and condensation

The scheme for computing the convective temperature changes consists of a so-called "moist convective" adjustment and a "dry convective" adjustment. The dry convective adjustment is performed if the lapse rate becomes superadiabatic. The lapse rate is adjusted to the dry adiabatic lapse rate so as to simulate the effects of strong mixing by free dry convection in the free atmosphere. This adjustment is performed in the model in such a way that the sum of potential and internal energies are conserved.

One of the most serious difficulties in designing a numerical model of the general circulation is in the parameterization of moist convection. Since we know very little about the interaction of small-scale convection with the large-scale fields of motion, we adopted an extremely simple system for simulating the effect of moist convection on the macroscopic behavior of the atmosphere. It is essentially similar to the moist convective adjustment proposed by Manabe *et al.* (1965) except that the critical relative humidity and critical static stability for moist convection are altered. Despite its simplicity, this system qualitatively possesses at least some of the essential characteristics of moist convection in the actual atmosphere. A brief description of the scheme follows.

The conditions for the onset of moist convection are

$$h>h_c, \tag{22}$$

$$-\frac{\partial T}{\partial p}>\Gamma_c, \tag{23}$$

where h is relative humidity, and h_c is critical relative humidity for moist convection, assumed to be 0.85 for this model. The critical lapse rate Γ_c is defined by (29).

If these conditions are satisfied, it is assumed that free moist convection is intense enough to make the partial equivalent potential temperature, Θ_{ep}, and relative humidity constant in the convective layer, i.e.,

$$\frac{\partial \Theta_{ep}}{\partial p}=0, \tag{24}$$

$$h=h_c, \tag{25}$$

where

$$\Theta_{ep}=\Theta e^{Lr_c/(c_pT)}. \tag{26}$$

The critical mixing ratio r_c is defined by

$$r_c=\frac{0.622[h_c e_s(T)]}{p-[h_c\cdot e_s(T)]}\approx h_c r_s, \tag{27}$$

where Θ is potential temperature, L the latent heat of condensation, $e_s(T)$ the saturation vapor pressure, and r_s the saturation mixing ratio of water vapor. In addition, it is assumed that total energy is unaltered by the process of moist convection, i.e.,

$$\int_0^{p_s}(c_p\delta T+L\delta r)dp=0, \tag{28}$$

where δT and δr denote the convective adjustment of temperature and mixing ratio of water vapor, respectively. The critical lapse rate Γ_c which satisfies (24) and (25) is given by

$$\Gamma_c=-g\frac{R}{c_p}\frac{T}{p}\left[\frac{p+0.622\dfrac{Lh_c e_s(T)}{RT}}{p+0.622\dfrac{L}{c_p}h_c\dfrac{\partial e_s(T)}{\partial T}}\right], \tag{29}$$

where

$$\frac{\partial e_s(T)}{\partial T}\approx\frac{Le_s(T)}{R_v T^2}, \tag{30}$$

R is the gas constant of dry air (0.287 J gm^{-1} K^{-1}) and R_v the gas constant of water vapor (0.461 J gm^{-1} K^{-1}). Since $1.0\geqslant h_c>0$, Γ_c lies somewhere between the moist and dry adiabatic lapse rates.

The net effect of the moist convective adjustment described above is to stabilize the lapse rate, condense water vapor, release the heat of condensation, and transfer heat from the lower to the upper layer. Further details of the moist convective scheme, in which the parameter h_c is assumed to be 1, may be found in Manabe *et al.* (1965).

If the tentative lapse rate is not supercritical, condensation will still be forecast to occur in the model atmosphere whenever the tentative mixing ratio exceeds the critical relative humidity h_c. At each level of supercritical humidity, changes of temperature and mixing ratio are determined from the simultaneous solution of a pair of equations by an iterative method. For simplicity in the computation scheme, all condensation resulting from this procedure is assumed to fall out of the atmosphere immediately, and no condensation goes into clouds or evaporates while falling through drier lower layers. Differentation between rain or snow depends upon the temperature at a height of about 350 m. This height is selected subjectively by reference to a survey article by Penn (1957). If the temperature at this level is freezing or below, snow is forecast; otherwise, rain is predicted.

e. Subgrid-scale mixing

1) HORIZONTAL MIXING

The formulation of the horizontal subgrid-scale mixing is an adaptation of the scheme used by Smagorinsky *et al.* (1965). According to Smagorinsky (1963), the rates of change of the east-west and north-south momentum, resulting from the horizontal stresses appearing in (1) and (2), are computed as

$${}_HF_\lambda=\frac{\partial\tau^{\lambda\lambda}}{a\cos\theta\partial\lambda}+\frac{\partial(\tau^{\lambda\theta}\cos^2\theta)}{a\cos^2\theta\partial\theta}, \tag{31a}$$

$${}_HF_\theta=\frac{\partial\tau^{\theta\lambda}}{a\cos\theta\partial\lambda}+\frac{\partial(\tau^{\theta\theta}\cos\theta)}{a\cos\theta\partial\theta}+\frac{\tan\theta}{a}\tau^{\lambda\lambda}, \tag{31b}$$

where $\tau^{\lambda\lambda}$, $\tau^{\lambda\theta}$, $\tau^{\theta\lambda}$ and $\tau^{\theta\theta}$ denote the stress tensors resulting from mixing along constant σ-surfaces. Ignoring the density variation on a constant σ-surface and assuming the hydrostatic relationship, we can express the stress tensors by

$$\tau^{\lambda\lambda}=-\tau^{\theta\theta}=p_* K_H D_T, \tag{32a}$$

$$\tau^{\lambda\theta}=\tau^{\theta\lambda}=p_* K_H D_s, \tag{32b}$$

where the tension and shearing rates of strain, respectively, are defined as

$$D_T=\frac{\partial u}{a\cos\theta\partial\lambda}-\frac{\cos\theta}{a}\frac{\partial}{\partial\theta}\left(\frac{v}{\cos\theta}\right), \tag{33a}$$

$$D_s=\frac{\partial v}{a\cos\theta\partial\lambda}+\frac{\cos\theta}{a}\frac{\partial}{\partial\theta}\left(\frac{u}{\cos\theta}\right). \tag{33b}$$

The assumption of an inertial subrange for energy cascade by three-dimensional turbulence yields the following relation by dimensional analysis[2]:

$$K_H=l_H^2|D|, \tag{34}$$

where $|D|=(D_T^2+D_s^2)^{\frac{1}{2}}$ and l_H is a characteristic length corresponding to the scale that defines the exchange coefficient. This length is assumed to be defined as

$$l_H=k\delta_s, \tag{35}$$

where the parameter k is assigned the value 0.2 and the mean grid distance δ_s is computed by

$$\delta_s=\tfrac{1}{2}(\delta_{s\lambda}+\delta_{s\theta}). \tag{36}$$

[2] The formulation of subgrid-scale mixing adopted in this study is obtained from the assumption of the inertial subrange for energy cascade by three-dimensional turbulence. Recently, Leith (1969) proposed an alternate formulation assuming the existence of the inertial subrange for enstrophy cascade by quasi-two-dimensional turbulence. It may be more reasonable to use his formulation rather than the present one because the grid box is quasi-two-dimensional (i.e., the horizontal grid size is much greater than vertical grid size). His formulation is being tested at the present time.

The latitudinal and longitudinal grid sizes are defined by

$$\delta_{s\lambda}=a\Delta\theta, \tag{37a}$$

$$\delta_{s\theta}=\begin{cases} a\cos\theta\Delta\lambda, & \theta<\theta_c \\ L_{\min}/2, & \theta>\theta_c \end{cases} \tag{37b}$$

The above equation implies that, in the region of Fourier filtering ($\theta>\theta_c$), half of the length of the shortest wave retained is regarded as an equivalent grid size (see Section 2d for the definition of $L_{\min}$ and θ_c).

For the formulation of subgrid-scale mixing of heat and moisture, we assume that these properties are mixed on isobaric instead of on σ-surfaces. The approximate equation for computing the contribution of horizontal mixing to the change of temperature or mixing ratio of water vapor is

$${}_HF_\alpha\approx\frac{\partial}{a\cos\theta\partial\lambda}\left[p_*K_H\left(\frac{\partial\alpha}{a\cos\theta\partial\lambda}\right)_p\right]+\frac{\partial}{a\cos\theta\partial\theta}\left[p_*K_H\cos\theta\left(\frac{\partial\alpha}{a\partial\theta}\right)_p\right], \tag{38}$$

where α stands for either temperature or mixing ratio. For a more general form of this equation, refer to Kurihara and Holloway (1967).

2) Vertical mixing

The formulation of the vertical mixing of momentum used in this work is identical to that described by Smagorinsky *et al.* (1965). The frictional force produced by this vertical mixing of momentum is computed by

$$\frac{{}_v\mathbf{F}}{p_*}=\frac{1}{\rho}\frac{\partial{}_v\boldsymbol{\tau}}{\partial z}, \tag{39}$$

where ρ and g are the density of air and the acceleration of gravity, respectively. The components of the vector ${}_v\mathbf{F}$ are ${}_vF_\lambda$ and ${}_vF_\theta$ appearing in (1) and (2). The stress on a horizontal surface ${}_v\boldsymbol{\tau}$ is computed by

$${}_v\boldsymbol{\tau}=\rho K_v\frac{\partial\mathbf{V}}{\partial z}, \tag{40}$$

where the coefficient of vertical diffusion K_v is based on the mixing length hypothesis, namely,

$$K_v=l_v^2\left|\frac{\partial\mathbf{V}}{\partial z}\right|. \tag{41}$$

The vertical mixing length l_v is assumed to increase linearly with respect to height up to 75 m and then to decrease linearly with height to 2.5 km where it becomes zero. Therefore, no subgrid-scale vertical mixing is assumed to occur above 2.5 km. The value of l_v at 75 m is assumed to be 30 m (this implies that the von Kármán constant is equal to 0.4 below 75 m). The equation for computing the stress at the lower boundary is presented in Section 2f.

The rate of temperature change due to vertical mixing is computed by

$$\frac{{}_vF_T}{p_*}=\frac{1}{c_p\rho}\frac{\partial H}{\partial z}, \tag{42}$$

$$H=\rho K_v\frac{\partial(T+\Gamma_d z)}{\partial z}, \tag{43}$$

where

$$\Gamma_d=g/c_p, \tag{44}$$

z is height above sea level, Γ_d the dry adiabatic lapse rate, and K_v the vertical eddy mixing coefficient.

The vertical diffusion of mixing ratio in this model is the same as described by Manabe *et al.* (1965). The change in mixing ratio due to small-scale vertical mixing is given by

$$\frac{{}_vF_\tau}{p_*}=\frac{1}{\rho}\frac{\partial W}{\partial z}, \tag{45}$$

$$W=\rho K_v\frac{\partial r}{\partial z}. \tag{46}$$

f. Boundary conditions at the earth's surface

The surface stress in the model is computed by

$$\boldsymbol{\tau}_*=-\rho(h)C_D(h)|\mathbf{V}(h)|\mathbf{V}(h), \tag{47}$$

where $C_D(h)$ is the drag coefficient applicable to winds at height h and is defined as

$$C_D(h)=[k_0/\log_e(h/z_0)]^2, \tag{48}$$

and where $\rho(h)$ is density, $\mathbf{V}(h)$ the velocity at height h, and k_0 the von Kármán constant, assumed to be 0.4. The roughness parameter z_0 is chosen to be 1 cm, and h is the height of the lowest prognostic level. The surface stress thus computed constitutes the lower boundary condition for the computation of the Reynolds stress resulting from vertical mixing.

Similarly, the heat flux $({}_vH)_*$ at the surface of the earth for either land or sea is given by the relation

$$({}_vH)_*=c_p\rho(h)C_D(h)|\mathbf{V}(h)|[T_*-T(h)/\sigma(h)^{h/c_p}], \tag{49}$$

where T_* is the surface temperature. For insuring that a minimum amount of heat is exchanged between the earth's surface and the lowest level of the model atmosphere, the wind speed $|\mathbf{V}(h)|$ used in (49) is not allowed to be less than 1 m s^{-1}.

The flux of latent energy $({}_vLH)_*$ from the ocean is obtained from

$$({}_vLH)_*=LE, \tag{50}$$

$$E=\rho(h)C_D(h)|\mathbf{V}(h)|[r_s(T_*)-r(h)], \tag{51}$$

where L is the latent heat of evaporation (sublimation), E the rate of evaporation (sublimation), and $r_s(T_*)$ the saturation mixing ratio of water vapor over water (ice) at the surface temperature. Over land, E is computed from (51) only when the surface is sufficiently wet. The formula for estimating the rate of evaporation from a drier surface is discussed in the following section. The heat and moisture fluxes at the earth's surface constitute the lower boundary conditions for the computation of the vertical mixing of heat and moisture.

To compute heat flux $({}_vH)_*$ and moisture flux E, it is necessary to know the surface temperature T_*. The surface temperature of the ocean is predicted by the thermodynamic equation of the ocean model. Over the continents, T_* is determined such that it satisfies the requirement of a surface heat balance. If we assume that the heat capacity of the land surface is zero (i.e., no heat conduction into the soil), the equation of the heat balance requirement is

$$S_*+(DLR)_*=\sigma_{SB}T_*^4+({}_vH)_*+({}_vLH)_*, \quad (52)$$

where S_* and $(DLR)_*$ are the net downward insolation and the downward longwave radiation at the earth's surface, respectively, and σ_{SB} is the Stefan-Boltzmann constant. Since the diurnal variation of insolation is eliminated in the model, we assume that it is therefore justifiable to neglect heat conduction into the soil. The heat balance equation (52) is solved with respect to T_* numerically.

g. *Hydrology of land surface*

As we know, hydrological processes profoundly affect the climate by controlling evaporation from the earth's surface and by altering the area of snow cover which reflects a major part of solar radiation. Therefore, the formulation of ground hydrology constitutes an essential part of climate modeling. The formulation adopted for this model is essentially similar to that described by Manabe (1969a) except for some minor modifications. Using this scheme, Holloway and Manabe (1971) constructed a global model of climate and were successful in simulating many of the essential features of climate and hydrology in global scale despite the extreme idealizations adopted for this formulation. A brief description of the scheme follows.

The maximum amount of water that can be stored in the ground is called the field capacity of the soil of a particular area. The field capacity of soil depends upon a number of characteristics of the ground surface and thus varies considerably throughout the world. For the utmost simplicity we have set the field capacity of the soil to 15 cm over all land areas. Most of the time, the actual soil moisture at a given point falls short of the field capacity of the soil in that area. In the model, a budget of soil moisture is kept at each land grid point. Over all land points, the soil moisture was initially set to its full capacity of 15 cm. Changes in soil moisture are computed as the residual of contributions from processes that increase soil moisture (i.e., rainfall and snowmelt) and those that decrease it (i.e., evaporation and runoff). Runoff is predicted at a grid point only if a forecast change in soil moisture would result in a water depth exceeding the field capacity. Runoff is assumed to flow directly to the sea via rivers without affecting the soil moisture at any other point. Rivers are assumed to flow from higher to lower terrain elevations in the direction of maximum surface slopes. The runoff from the continents into the sea determines the location and rate of the supply of fresh water to the ocean.

The effect of soil moisture on evaporation is incorporated into the model by a simple scheme used by Budyko (1956). When the soil does not contain a sufficient amount of water, the amount of evaporation is smaller than the value obtained from (51), which gives the rate of evaporation from the sea or a perfectly wet surface. If the soil moisture is greater than a certain critical percentage (75% in this study) of the maximum soil capacity, evaporation is computed from (51). Otherwise, evaporation from land is computed to be linearly proportional to soil moisture up to this critical value.

The equation for the prediction of the water equivalent depth of snow S is

$$\frac{\partial S}{\partial t}=S_F-E-M_e, \quad (53)$$

where S_F is the rate of snowfall, M_e the rate of snowmelt, and E the sublimation rate. The snowmelt rate may be calculated from a heat balance condition at the snow-covered surface as

$$M_e=\begin{cases}\dfrac{E_x}{L_f}, & \text{if } E_x>0\\ 0, & \text{if } E_x\leqslant 0\end{cases} \quad (54)$$

where L_f is the latent heat of fusion, and E_x, the rate of excess heat energy made available for melting snow, is computed from

$$E_x=[S_*+(DLR)_*-\sigma_{SB}T_*^4 -({}_vH)_*-({}_vLH)_*]_{T_*=273.2\text{K}}, \quad (55)$$

with T_* at the freezing point. The heat flux terms $({}_vH)_*$ and $({}_vLH)_*$ are expressed by (49) and (50). Refer to Manabe (1969a) for further details of the hydrologic processes in the model.

h. *Interaction with the ocean*

The joint ocean-atmosphere model is constructed by combining the atmospheric model just described and the oceanic model described in Part II. They are coupled with each other as proposed by Manabe and Bryan (1969). Fig. 4 indicates schematically the interaction

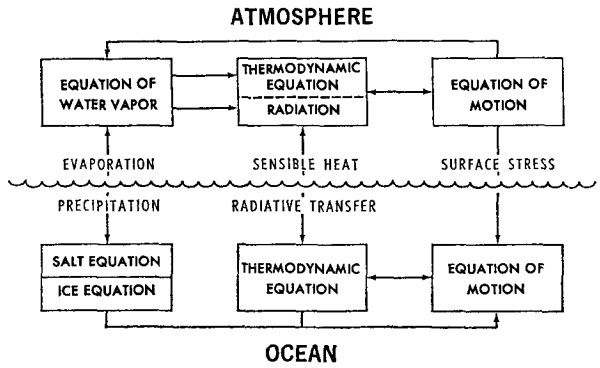

FIG. 4. Diagram of the coupling of the major components of the joint ocean-atmosphere model.

among the major components of the joint model. In this section, we shall describe how these components interact with each other.

The average temperature of the upper 50 m of the ocean is taken to be representative of the surface mixed layer. The temperature of this surface layer is used as the lower boundary condition of the atmospheric model. The rates of supply of heat, momentum and water to the ocean surface, which are computed as described below, serve as the upper boundary condition for the ocean model.

1) HEAT EXCHANGE

The heat balance components that affect the heat balance of the ocean surface are solar radiation, terrestrial radiation, and fluxes of sensible and latent heat due to turbulence, which are computed in the atmospheric part of the joint model using the sea surface temperatures obtained from the oceanic part of the model (see Section 2c for further details of the flux computation). The rate of energy received by the ocean surface is the net contribution of the fluxes mentioned above.

When ice covers the ocean surface, the temperature of the ice surface is computed in a way similar to that of soil surface by solving (52), except that the heat conduction into the ice is taken into consideration. If the surface temperature thus determined is above freezing, it is assumed that the ice surface has a freezing temperature and the excess heat is used for melting of the ice. Given the temperature of the ice surface, one can determine the rate of heat conduction through ice, which constitutes the thermal boundary condition for the ice-covered ocean.

2) WATER EXCHANGE

In the joint model, the exchange of water and ice between ocean and atmosphere or between ocean and continent affects the distribution of salinity and sea ice in the ocean. The ocean gains water either through rainfall, the melting of sea ice or runoff from continents, and loses water either through evaporation or the freezing of water. The salinity of sea water is diluted or concentrated depending upon whether the ocean gains or loses water. The amount of sea ice increases either through snowfall, glacier formation or freezing, and decreases through sublimation or melting. Sections 2d, 2f and 2g describe how the rates of rainfall (snowfall), evaporation (sublimation), and runoff are computed. For the calculation of the rates of melting and freezing of sea ice, see Part II.

In order to prevent the snow from accumulating indefinitely over the continents, we introduced a highly idealized mechanism of glacier formation. If the snow depth exceeds a certain critical depth, i.e., 20 cm of water equivalent, snow is assumed to form glaciers which in turn move toward the coastal region and become sea ice. The direction of glacier movement is assumed to be identical with that of water runoff described in Section 2g. While it is obvious that glaciers cannot form during short periods, this idealized mechanism of glacier formation is introduced to obtain a quasi-steady state of the distribution of snow depth.

3) MOMENTUM EXCHANGE

The exchange of momentum is computed from (47). The effect of ocean currents on the momentum exchange is neglected, since the velocity of ocean currents is much smaller than the velocity of air flow. Also any dependence of surface roughness (i.e., C_d) on wind speed is neglected.

i. Approach to equilibrium

We have attempted to simulate the global climate of the ocean-atmosphere system as the state of quasi-equilibrium that results from the time integration of the joint model. Since different types of fluid motion occur in the atmospheric and oceanic models, the atmospheric model requires approximately 300 times more computation to integrate over a given time period than the oceanic model. According to the results of the numerical integration of the atmospheric model, the thermal relaxation time of the atmosphere is of the order of 1 year. On the other hand, an estimate of the ratio of heating to the heat capacity of the ocean indicates that the thermal relaxation time of the ocean is of the order of centuries. Obviously, it was not feasible to make a straightforward integration of the interacting models over a long enough period for the oceanic part of the model to reach adjustment. In order to optimize the amount of computation, the method of time integration proposed by Manabe and Bryan (1969) is used. For example, the coupling between the atmospheric part and the oceanic part of the model is adjusted such that the evolution of the former during one atmospheric year is coupled with that of the latter during 320 years. In other words, the atmosphere

at year 0, 0.5 and 1.0 interacts with the ocean at year 0, 160 and 320 of the time integration, respectively.

The rates of supply of heat, momentum and water to the ocean surface, which are computed in the atmospheric model, serve as the upper boundary condition for the oceanic model. A running time-mean operator is applied to the vertical fluxes to avoid an overresponse of the oceanic model to features caused by individual synoptic disturbances in the atmospheric model. For the details of this time-mean operator, see Manabe (1969b).

At the start of the time integration, both the atmosphere and the ocean are at complete rest. The atmosphere is isothermal with a temperature of 288K and contains no moisture. The ocean is stably stratified such that surfaces of constant temperature and salinity are horizontal. The joint ocean-atmosphere model was integrated in time for a total of 310 atmospheric model days, which corresponds to 272 oceanic model years. In order to show the evolution of the heat balance of the joint system, the time variations of the global mean net radiation fluxes at the top of the atmosphere are shown in the upper half of Fig. 5 for the entire period of the time integration. The converging values of global mean longwave and solar radiation indicate that the joint system as a whole is very close to the state of thermal equilibrium toward the end of the integration period. A discussion of the thermal equilibrium of the oceanic model will be given in Part II. The lower half of Fig. 5 shows how the mean temperature of the model atmosphere approaches the final state from the initial isothermal condition.

3. The A-model

As discussed in the Introduction, the major objective of this study is to identify the climatic effects of the heat transport by ocean currents. In order to do this, the climate from the joint ocean-atmosphere model is compared with the climate of the so-called "A-model" in which the effects of ocean currents are not taken into consideration. By identifying the differences between these two climates, one can speculate the effects of ocean currents upon the climate. A very brief description of the A-model[3] follows.

The basic difference between the joint model and the A-model lies in the modeling of the ocean. In the A-model, the ocean is assumed to be a completely wet surface without any heat capacity. This idealized ocean resembles a swamp. The surface temperature of the ocean is computed from (52) in the same manner as the temperature of the continental surface. It is determined such that it satisfies the assumption of zero heat capacity. In short, the ocean of the A-model resembles the actual ocean in that it can be an unlimited source of water for the atmosphere but lacks the effects of heat transport by ocean currents. Except for the idealization of the ocean, the structure of the A-model is identical to that of the joint model.

The numerical time integration of the A-model is carried out for the period of 300 model days. The initial condition for this integration is a resting state with a uniform temperature of 288 K and no moisture. This is identical with the initial atmospheric state for the time integration of the joint model.

4. Discussion of results

In this section the results from both the atmospheric part of the joint model and from the A-model atmosphere are presented. For the joint model the data shown are the time mean for the 60-day period beginning at day 251. Results for the A-model are the time mean of the 60-day period commencing at day 241. As explained in the preceding section, the two climates obtained are compared extensively. Although we have not carried out a careful examination of the statistical significance of the differences between the two time mean states,[4] it is encouraging that many of the differences identified here qualitatively agree with those suggested earlier by Manabe (1969b) and Bryan (1969). Whenever possible, results from both models are compared with the annual mean state of the actual atmosphere.

a. Temperature

The latitude-height distribution of the zonally averaged temperature computed by the joint model is shown in the upper half of Fig. 6. The general qualitative features of this distribution are similar to those of the annual mean state of the actual atmosphere. The latitude-height distribution of the difference between the temperatures of the joint model and A-model atmospheres is shown in the lower half of Fig. 6. In higher latitudes, except for the polar regions, the tropospheric temperature of the joint model is warmer than that of the A-model. On the other hand, the former is slightly colder than the latter in low latitudes. The poleward transport of heat by ocean currents, discussed in Section 4e, is responsible for these differences. Fig. 6 also indicates that the cooling effect of ocean circulation extends vertically throughout the troposphere in the tropics, whereas the warming effect in higher latitudes is limited mostly to the lower troposphere and its

[3] Manabe (1969a) constructed a model which is similar to the A-model except that it has highly idealized geography. Refer to his paper for further details of the structure of this model.

[4] In order to firmly establish the significance of the difference between the two model climates, it is necessary to ascertain that the amplitude of the fluctuation of the 60-day mean climate is less than the magnitude of the difference between the two 60-day mean states described here. Recently, the study of Leith (1973) came to our attention. By using the concept of signal-to-noise ratio, he developed a framework which may be useful for our purpose. It is planned to use his method for the evaluation of the results from the final experiment with high computational resolution.

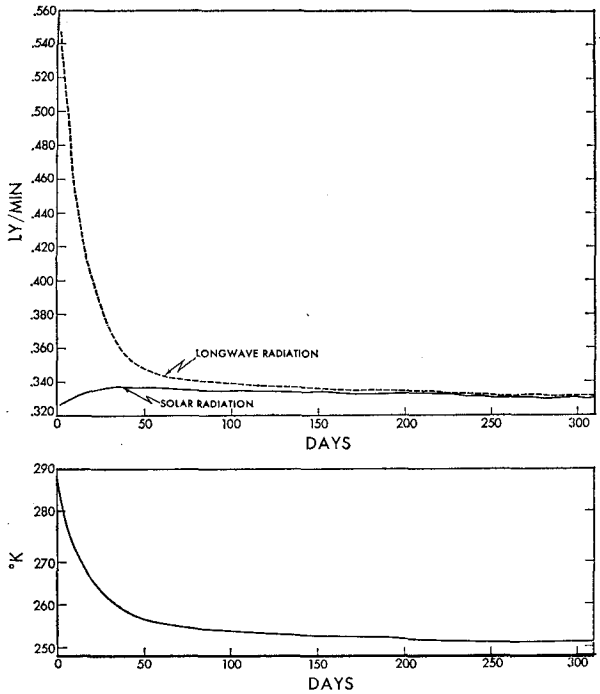

FIG. 5. Time variation of the global mean net radiation at the top of the atmosphere (ly min^{-1}), and the mean mass-weighted temperature of the atmosphere for the joint model (K).

magnitude is very large. This occurs because the energy input from the ocean surface spreads throughout the troposphere by moist convection in the tropics, whereas, in higher latitudes it is contained in the lower troposphere due to the stable stratification of the air mass. Furthermore, the poleward transport of heat by ocean currents causes the melting of snow cover and sea ice, markedly reduces the albedo of the earth's surface poleward of 55° latitude, and thus magnifies the warming there. Since the lower tropospheric warming is much larger than the cooling in the tropics, the overall effect of ocean circulation is to increase the area mean temperature in the lower troposphere. An essentially similar conclusion was obtained in the earlier study by Manabe (1969b). In the upper troposphere and stratosphere, the temperature change caused by the ocean circulation is small but seems to be significant. For example, in the tropics, the temperature of the stratosphere increases slightly due to the effects of ocean currents in contrast to the tropospheric cooling mentioned earlier. This is a consequence of the stronger upward motion in the A-model tropics, which allows more adiabatic cooling to occur in the lower stratosphere of the tropics. (Refer to Section 4b for a description of the distributions of meridional circulation in both models.)

The global distribution of temperature at the lowest level of both the joint model atmosphere and the A-model atmosphere is shown in Fig. 7. For verification of the joint model, the observed distribution of annual mean surface air temperature (Crutcher and Meserve, 1970; Taljaard *et al.*, 1969) is also added to the same figure. By comparing the distribution of the joint model with that of the A-model, one can infer the effects of oceanic heat transport on the surface air temperature. For example, the area of relatively low surface air temperature in the equatorial region of the eastern Pacific is found in the distribution of the joint model but is missing from the A-model. The upwelling of cold water in the joint model ocean is responsible for this difference. The intensity of upwelling, however, is not strong enough, partly because the surface easterlies around the equator are too weak. Therefore, the low temperature area of the joint model is less distinct than the actual area.[5] In middle latitudes of the joint model, the meridional temperature gradient is particularly large over the western portion of the North Pacific Ocean, where cold water flowing southward in the subarctic gyre meets the warm water flowing northward in the Kuroshio current. Again, this feature is missing in the distribution of the A-model due to the lack of oceanic heat transport. A similar concentration of isotherms is observed in the western part of the Atlantic Ocean. The joint model, however, fails to simulate this feature satisfactorily. Furthermore, the surface air temperature is too low in the northeastern part of the Atlantic Ocean of the joint model. These discrepancies may result from the fact that the Icelandic low and, accordingly, the subarctic gyre of the Atlantic are too weak. In the Arctic, the surface air temperature of the joint model is significantly lower than that of the actual atmosphere. This partly results from the excessive growth of the thickness of sea ice, which prevents the heat conduction from underlying water to the top surface of the ice. (Note that the surface air temperature in the polar region of the joint model is hardly warmer than that of the A-model.)

Fig. 8 depicts quantitatively the effect of the ocean circulation on the overlying air temperature. This figure shows the temperature difference between the two models at the lowest level of the model atmosphere. Compared to the A-model, temperatures of the joint model are cooler along the equator, due to the effect of ocean water upwelling, and much warmer at high latitudes over the oceans. As an example of the modification of atmospheric temperature by the oceans, consider the North Pacific Ocean and its surrounding land areas. A considerable warming has occurred over the northeastern boundary of the Pacific and northern portion of the North American Continent. Similar warming is evident over the northeastern region of the Atlantic Ocean and over western Europe. The northward transport of heat by the subarctic gyre is partly responsible for the warming in these regions. Furthermore, the general increase in land-sea contrast of surface

[5] See Fig. 7 of Part II for a similar comparison of sea surface temperature between the joint model and the actual atmosphere.

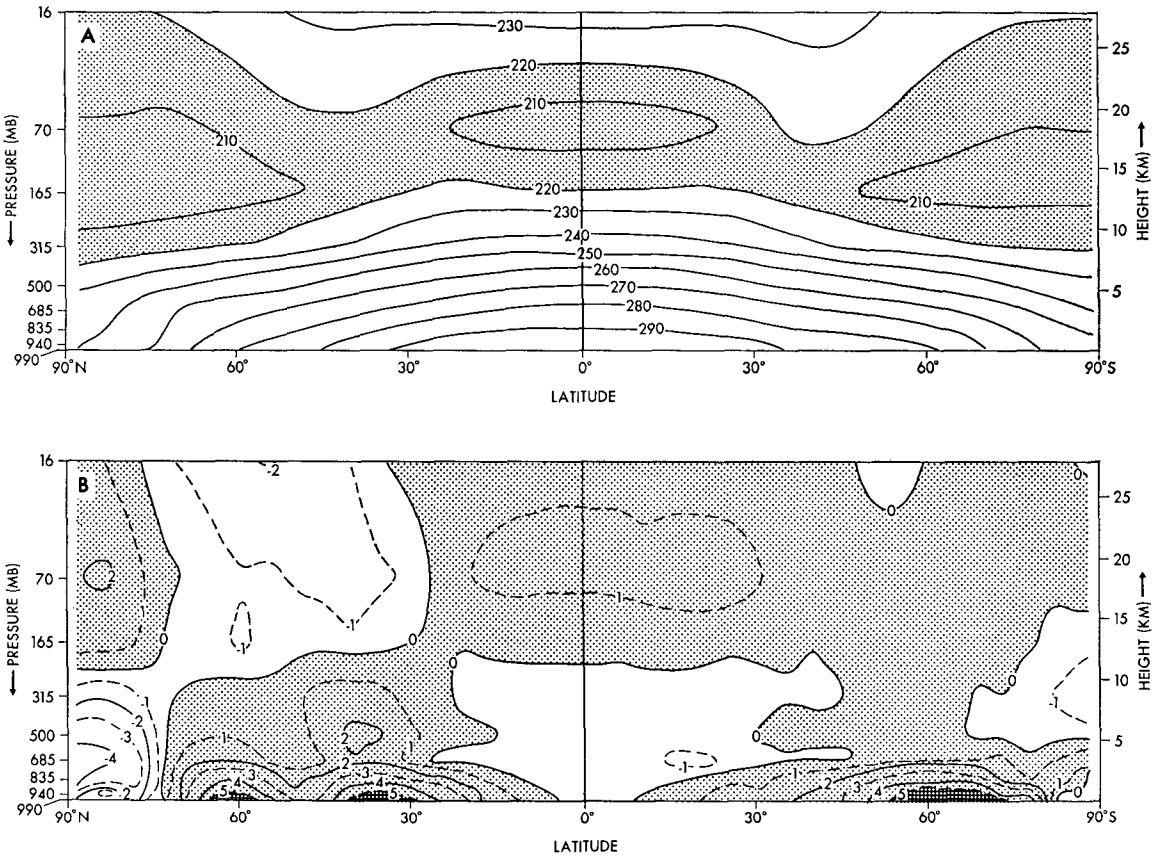

FIG. 6. Latitude-height distributions of the zonal mean temperature: (A) for the joint model atmosphere, and (B) the difference between the joint model and the A-model. Units, K.

temperature contributes to the intensification and the northward shift of the Aleutian low as discussed in Section 4c. These changes in the distribution of sea level pressure cause the southerlies to increase over the northwestern portion of the North American Continent and are responsible for raising the surface temperature there. The warming is further intensified by the increase of surface albedo caused by the melting of snow cover. Over the northeastern part of the Eurasian Continent, the surface air temperature is lowered significantly due to the effects of ocean currents. The northward shift and the intensification of the Aleutian low mentioned above increase the advection of cold air in this region and are responsible for this cooling. In lower latitudes, the northward advection of warm water by subtropical gyres accounts for the warming off the east coasts of Japan and the United States.

In the Southern Hemisphere, the sea surface temperature of the joint model is too high along the periphery of the Antarctic Continent because of the excessive warming due to the oceanic heat transport. As discussed in Part II, Ekman drift driven by the surface westerlies should have opposed the poleward movement of surface water and counteracted the poleward heat transport by the thermally-driven meridional circulation. Unfortunately, the intense surface westerlies (i.e., "roaring forties") which predominate in middle latitudes of the Southern Hemisphere are missing in the joint model, as discussed in Section 4c. Therefore, the oceanic heat supply to the coastal region of the Antarctic Continent is too large and is responsible for the exessive warming mentioned above. The warming is enhanced further by the melting of sea ice and the resulting reduction of surface albedo. This is why the meridional gradient of surface temperature in middle latitudes of the joint model is much smaller than the observed, as Fig. 7 indicates.

b. Zonal wind and meridional circulation

The latiude-height distribution of the zonal mean of the zonal wind in the joint model atmosphere is shown in the upper half of Fig. 9. The lower half of this figure shows the difference in the zonal wind between the joint model and the A-model. The intensity of the tropospheric zonal wind is significantly weaker in the joint model in the subtropics and most of the middle latitudes as a result of a general decrease in the meridional temperature gradient due to oceanic heat advection. Near the poles the westerlies are stronger in the joint

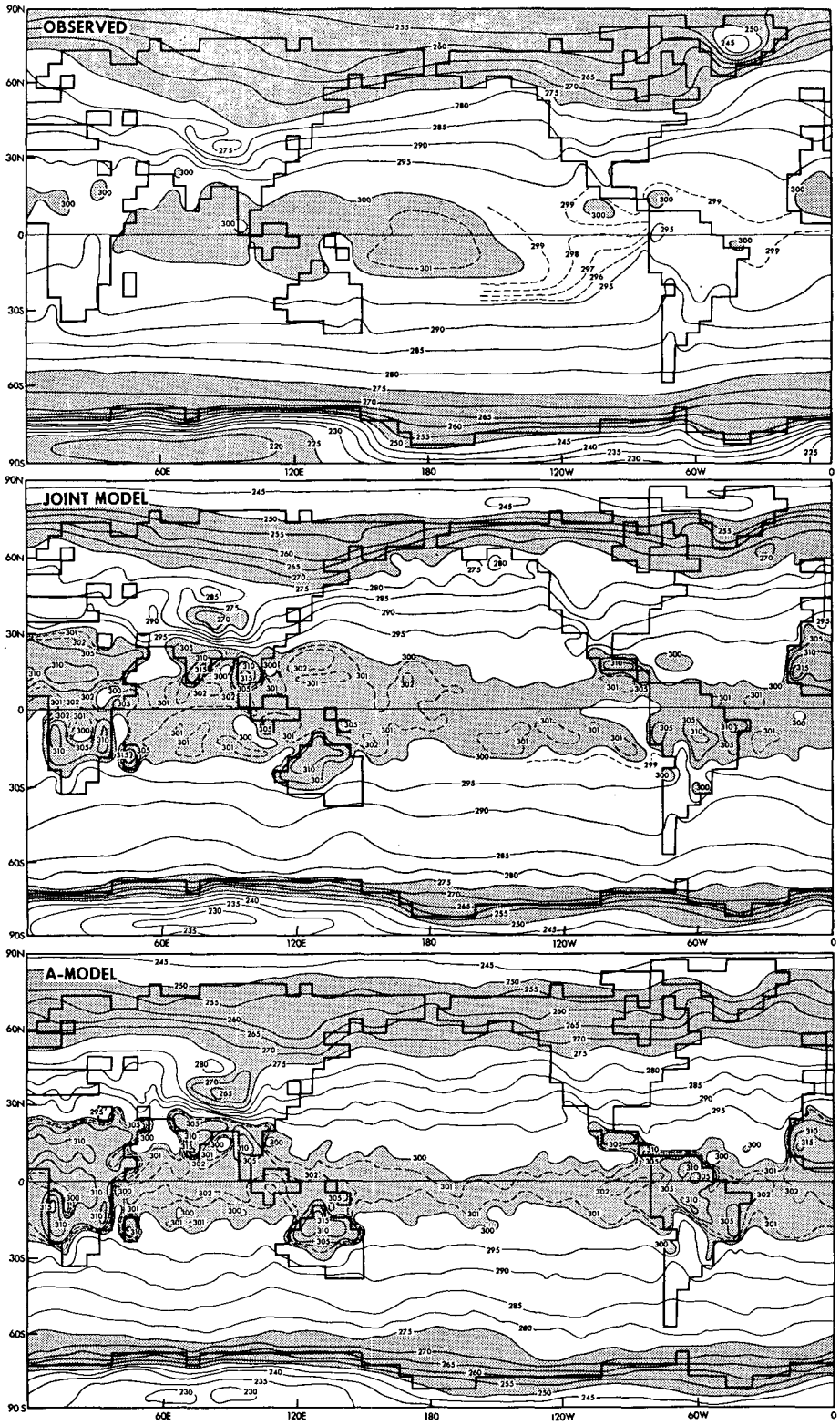

FIG. 7. Global distributions of annual average surface air temperature (K). Top: observed (Crutcher and Meserve, 1970; Taljaard *et al.*, 1969); middle: joint model; bottom: A-model. Computed temperatures are at the lowest level ($\sigma = 0.99$) of the model atmosphere.

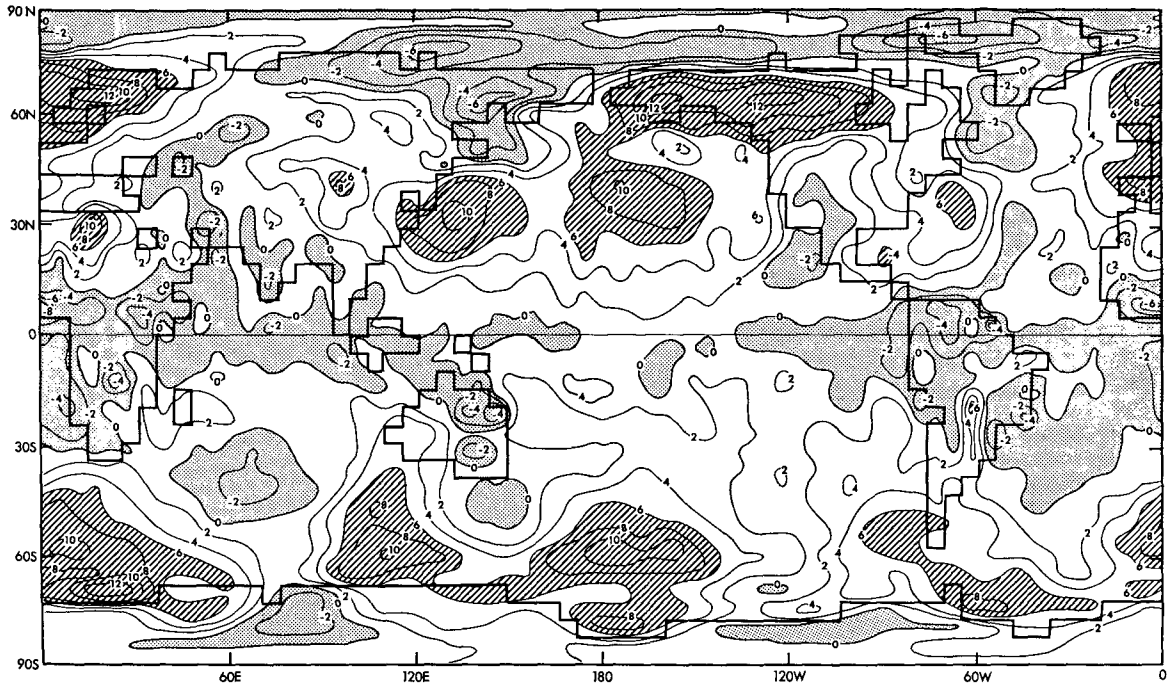

FIG. 8. Global distribution of the temperature difference (K) between the joint model and the A-model at the lowest level of the model atmosphere. Areas of temperature difference >6 K are cross-hatched, areas <0 are stippled.

model due to an increase in the meridional temperature gradient. This increase is due to the large temperature contrast between the cold polar regions and the warm surrounding oceans. According to the thermal wind relationship, the differences in the distribution of zonal wind described here are consistent with the differences in the zonal mean temperature which are shown in Fig. 6.

The streamfunctions of the meridional circulation in both the joint model and A-model are shown in Fig. 10. In both models the direct cell of the tropics, the indirect Ferrel cell of mid-latitudes, and the direct cell in the polar regions are evident. The intensities of the Ferrel cells in the joint model are weaker or less extensive than those in the A-model. As pointed out earlier, the poleward transport of heat by ocean currents reduces the meridional temperature gradient and, accordingly, the baroclinic waves which drive the indirect Ferrel circulation. Similar results were obtained from the earlier version of the joint model with idealized topography (Manabe, 1969b). Fig. 10 also indicates that the upward motion branch of meridional circulation in the tropics shifts northward and the mass transport in the branch decreases significantly due to the effect of ocean currents. This weakening results from the suppression of the tropical rainbelt by cold sea surface temperature which is discussed in Section 4d.

c. Sea level pressure

The latitudinal distribution of zonal mean sea level pressure for both models is compared with the observed in Fig. 11. The observed annual mean distribution was compiled from the data of Crutcher and Meserve (1970) and Taljaard *et al.* (1969). In both models the subtropical high and low pressure belts in both the tropics and mid-latitudes are present. However, the subtropical high and the mid-latitude low pressure belt are less developed in the joint model than in the A-model because of the generally weaker meridional temperature gradient in the joint model.

Unfortunately, the subtropical highs in the Southern Hemisphere of both models are too weak and are located in too low a latitude as compared with the observed distribution of sea level pressure. Furthermore, both models fail to simulate the large pressure gradient in middle latitudes of the Southern Hemisphere ("roaring forties") and the belt of low pressure along the periphery of the Antarctic Continent. These discrepancies seem to result from a combination of factors. Manabe *et al.* (1970) and Holloway and Manabe (1971) have shown that further decrease of the grid size for the horizontal finite differencing results in the intensification of the high pressure belt of the subtropics but does not sufficiently improve the simulation of the "roaring forties." On the other hand, Mintz (1965) was successful in simulating this feature and the belt of low pressure along the periphery of the Antarctic Continent by his two-layer model of the global circulation. So far, we have been unable to determine why the present model fails to reproduce these features.

The horizontal distributions of sea level pressure of both models are shown in Fig. 12 together with the

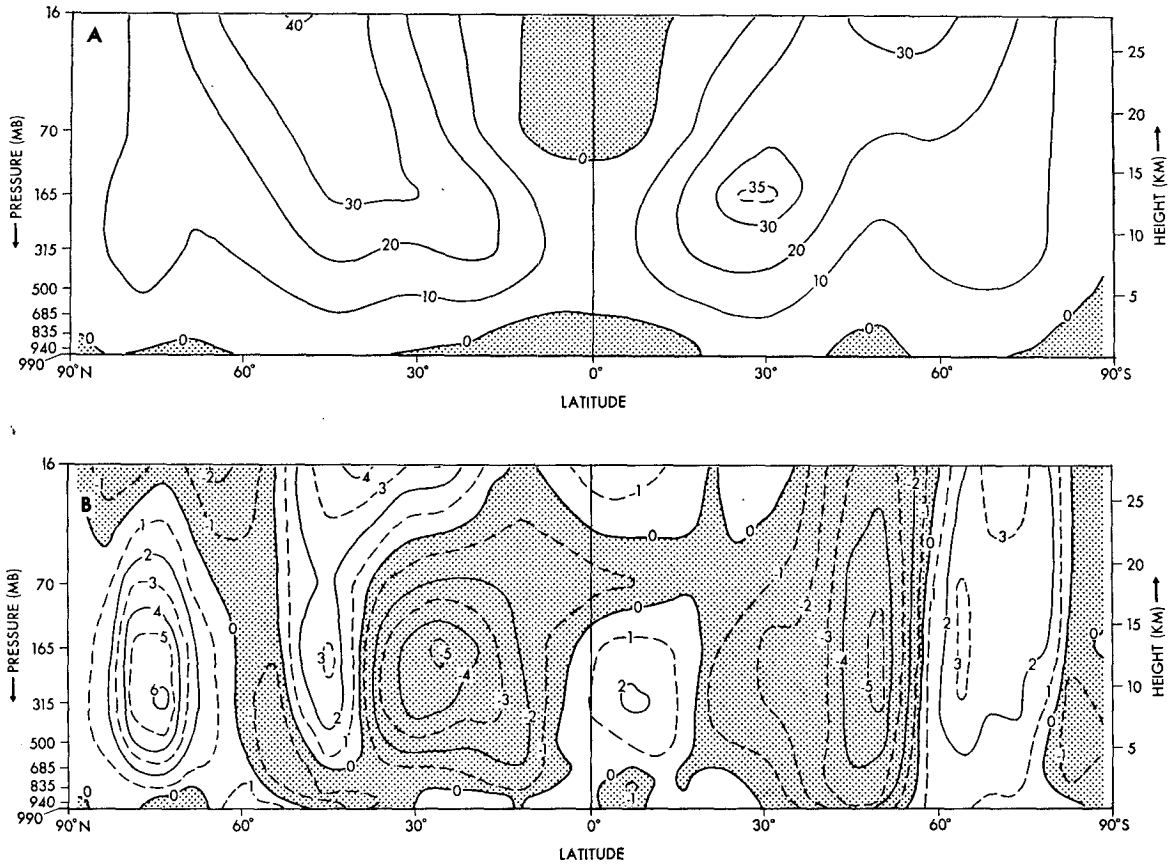

FIG. 9. Latitude-height distributions of (A) the zonally averaged zonal wind component (m s^{-1}) in the joint model atmosphere, and (B) the difference between the joint model and the A-model.

annual mean distribution in the actual atmosphere. Again, this comparison reveals the unrealistic features of the model atmospheres mentioned above. For example, the subtropical anticyclones in both model atmospheres are significantly weaker than those in the actual atmosphere. The belt of low pressure along the periphery of the Antarctic Continent is missing in the model distributions. Nevertheless, one can get some idea of the effects of ocean currents upon sea level pressure by comparing the two model distributions. According to this comparison, both the Aleutian and Icelandic lows as well as the Siberian high are intensified and shifted poleward by the effect of oceanic heat transport. Particularly, it is noteworthy that the Aleutian low changes fron split cyclones to a single cyclone. These changes probably result from the increase in the land-sea temperature contrast due to the poleward heat transport by ocean currents.

On the other hand, subtropical anticyclones over the oceans are weakened, due to the general reduction of baroclinicity as pointed out earlier. There are other differences between the distributions of the two models. However, detailed comparison does not seem to be warranted until a better simulation of sea level pressure is accomplished.

d. Water balance

In this section we discuss the effect of ocean circulation on the global distributions of precipitation and evaporation.

Fig. 13 shows the global distributions of precipitation for both models. The map of the observed rate of precipitation, which was compiled by Lvovitch and Ovtchinnikov (1964), is also added to this figure after smoothing out some small-scale features over continental regions. This figure indicates that the joint model partially simulates the areas of meager precipitation such as the Sahara Desert, Australia, and the southwestern part of the United States. However, these areas in the joint model are not as extensive as the actual regions, because the intensities of the subtropical highs and accompanying downward motion are significantly weaker than those of the actual atmosphere as discussed in the preceding section. Fig. 13 also indicates that the large-scale features of the tropical rainbelt are successfully simulated by the joint model. However, the distributions of precipitation in the tropics of both models include small-scale features which are not evident in the observed distribution. In view of the fact that these irregularities are often out of phase with the grid-scale

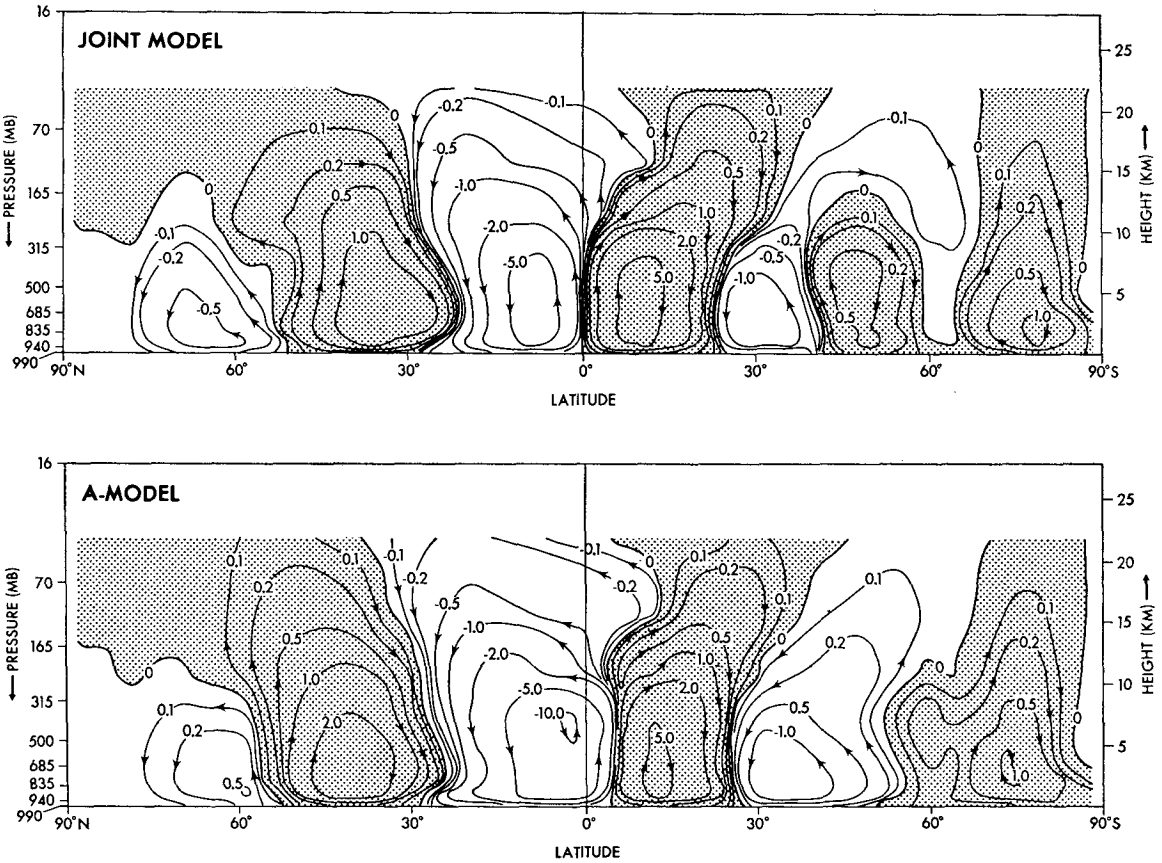

FIG. 10. Latitude-height distribution of the streamfunctions (10^{13} g $s^{-1} = 10^7$ tons s^{-1}) of the mean meridional circulation for the joint model atmosphere and the A-model. Positive areas are stippled.

variation in sea level pressure, it is probable that some of them are the manifestation of a computational mode contained in the model atmosphere.

The effects of the ocean circulation upon the distribution of precipitation can be identified by comparing the distributions of the precipitation rates of the two models which are shown in Fig. 13. For example, precipitation is suppressed by upwelling of cold water along the equator in the eastern Pacific Ocean and also along the west coasts of the continents at subtropical latitudes. The latter feature is evident in the coastal areas of Africa, Peru and California. These areas of meager precipitation, however, are not extensive enough compared to the observed rates. As mentioned in Section 4c and in Part II, the intensities of the subtropical highs and the induced coastal and equatorial upwelling are much weaker than the observed intensities. Accordingly, the sea surface temperature is not cold enough in these regions and accounts for these discrepancies.

In certain areas, ocean currents increase the rate of precipitation. The enhancement of rainfall can occur over regions of warm ocean water, which supplies heat and moisture to the overlying air and often enhances the development of disturbances. For example, the precipitation rate increases markedly off the coast of Japan and along the west coast of Canada where sea surface temperature increases due to oceanic heat transport (see Fig. 8).

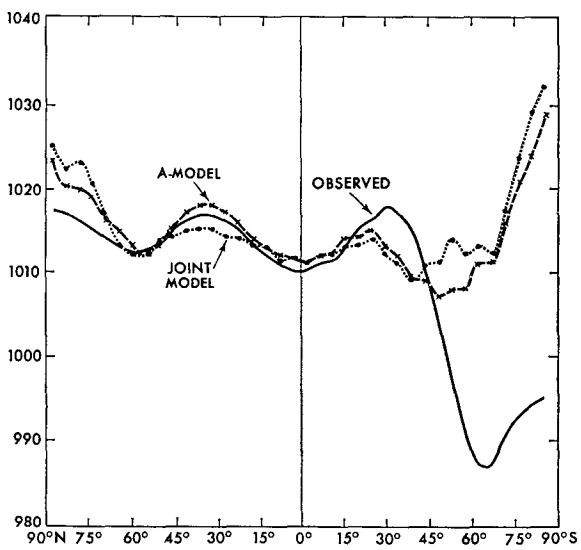

FIG. 11. Latitudinal distributions of the zonal mean sea level pressure (mb) for the actual atmosphere (Crutcher and Meserve, 1970; Taljaard *et al.*, 1969), the joint model, and the A-model.

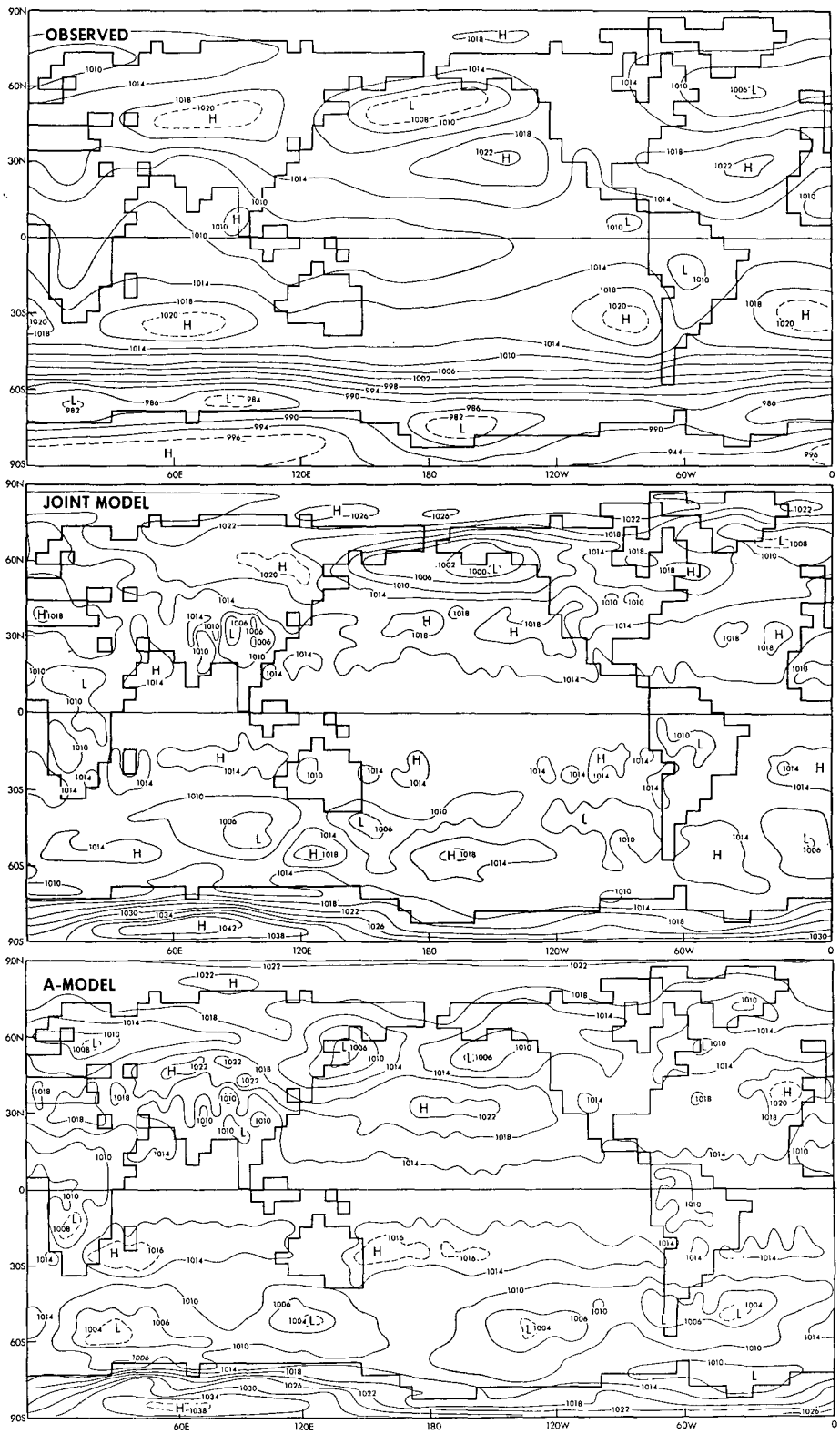

FIG. 12. Global distributions of sea level pressure (mb). Top: observed (Crutcher and Meserve, 1970; Taljaard *et al.*, 1969); middle: joint model; bottom: A-model.

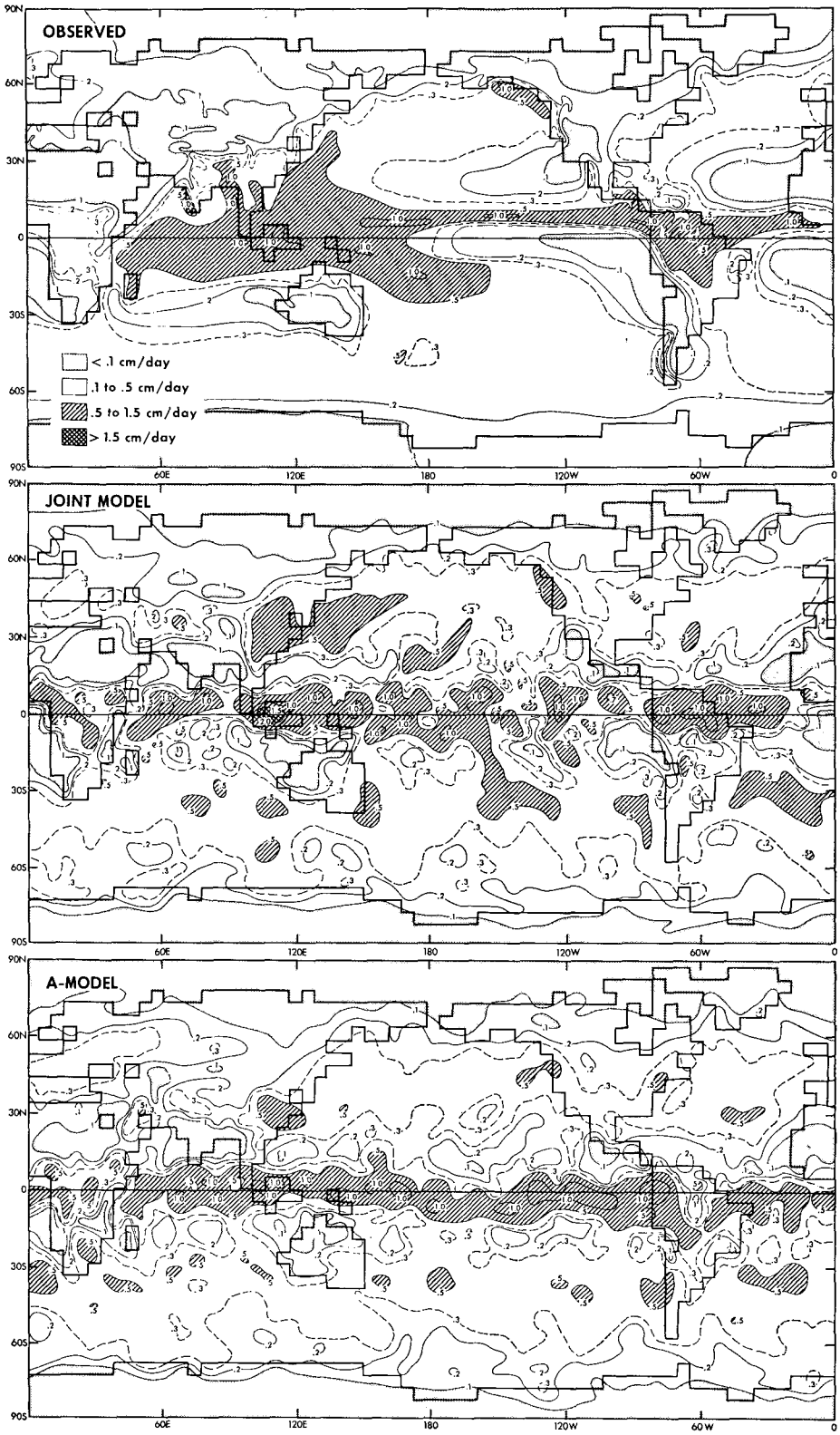

FIG. 13. Global distribution of precipitation rate (cm day^{-1}). Top: observed (Lvovitch and Ovtchinnikov, 1964); middle: joint model; bottom: A-model.

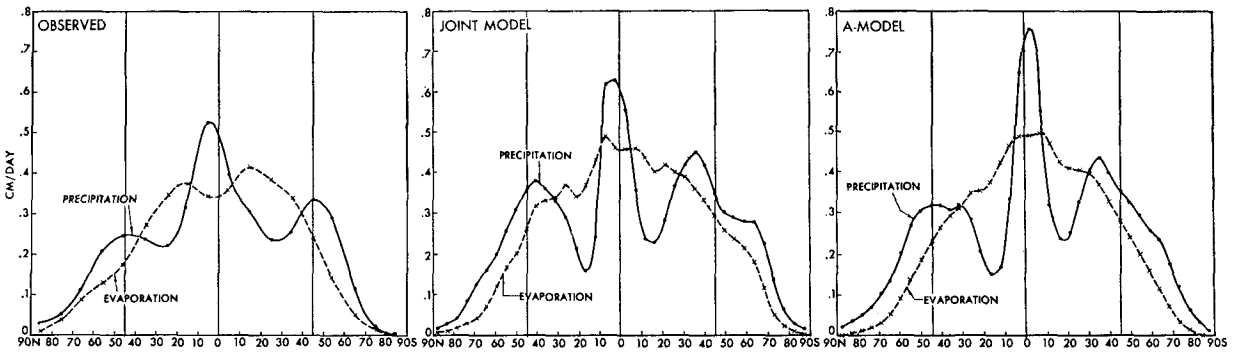

FIG. 14. Latitudinal distributions of the zonally averaged rates of precipitation and evaporation (cm day^{-1}). Left: observed (compiled by Sellers, 1965); middle: joint model; right: A-model.

Fig. 14 gives a quantitative comparison of the mean latitudinal distributions of precipitation and evaporation for the two models. The observed data are from Sellers (1965). One of the most significant effects of the ocean circulation on precipitation is clearly shown in the tropics. A reduction in the rainfall rate and a northward shift of the maximum rainfall have occurred in the joint model, compared to the A-model. A similar result was obtained by Manabe (1969b) from the earlier version of the joint model. As Fig. 7 indicates, the sea surface temperature along the equator generally decreases due to the upwelling of cold water. This cooling is responsible for the reduction of precipitation mentioned above. [For further discussion of this subject, see, for example, Bjerknes *et al.* (1969) and Manabe *et al.* (1974).]

According to Fig. 14, the belt of intense rainfall in the model tropics is significantly narrower than that in the actual tropics. This discrepancy is probably due to the assumption of no seasonal variation, which was adopted for the models. One should expect that the seasonal movement of the tropical rainbelt is partly responsible for widening the tropical maximum in the distribution of observed annual mean precipitation.

The global distribution of evaporation rate is given in Fig. 15, with observed data from Budyko (1963). The effect of ocean circulation is to suppress evaporation along the equator, where upwelling of cold ocean water occurs, and to increase evaporation over the predominately warm ocean currents that occur along the east coast of the continents. In general, the distribution of the evaporation rate of the joint model is more realistic than that of the A-model. However, the rate of evaporation around the equator is significantly larger than the observed.

The latitudinal distributions of evaporation rate (Fig. 14) show that although the pronounced minimum estimated by Sellers at the equator is missing in the joint model result, a reduction in the evaporation rate has occurred, compared to the A-model. As shown in Fig. 7, the surface air temperatures of the joint model near the equator are noticeably warmer than observed in the eastern Pacific Ocean and the Atlantic Ocean. Colder temperatures in these regions in the joint model should have the desired effect of suppressing evaporation and precipitation even further.

e. Heat balance

1) RADIATION BALANCE OF THE EARTH-ATMOSPHERE

The amount of net radiative flux at the top of the atmosphere determines the magnitude of the meridional transport of heat energy by the ocean-atmosphere system. The latitudinal distributions of the zonal mean net solar radiation and net longwave radiation at the top of the joint model atmosphere are given in Fig. 16. Observed values from Vonder Haar and Suomi (1971) are also plotted. In the mid-latitude regions of both hemispheres the radiative fluxes of the joint model agree well with the observed fluxes. In the Northern Hemisphere polar region, however, both solar and terrestrial fluxes are significantly less than the observed values due to high surface albedos and low surface temperature over the extensive snow and ice cover. Wetherald and Manabe (1972) pointed out that the lack of seasonal variation of solar insolation can be responsible for an excessive snow and ice cover. In the tropics, both solar and longwave fluxes in the joint model are generally less than the observed values. The cloud distributions used in the model may be somewhat inaccurate in this region. Despite various differences mentioned above, the net radiation flux (i.e., net downward solar flux minus net upward terrestrial flux) at the top of the atmosphere of the joint model agrees reasonably well with the net flux estimated by Vonder Haar and Suomi. This is because the differences in solar flux tend to compensate those in the flux of terrestrial radiation.

2) HEAT BALANCE OF THE EARTH'S SURFACE

On the continents at the surface of the earth, the contributions to the heat balance are the net radiative flux and the fluxes of sensible and latent heat. Over the oceans, in addition to these fluxes, heat is also supplied from the interior to the surface of the ocean in the joint model. This heat flux may be called "oceanic heat flux."

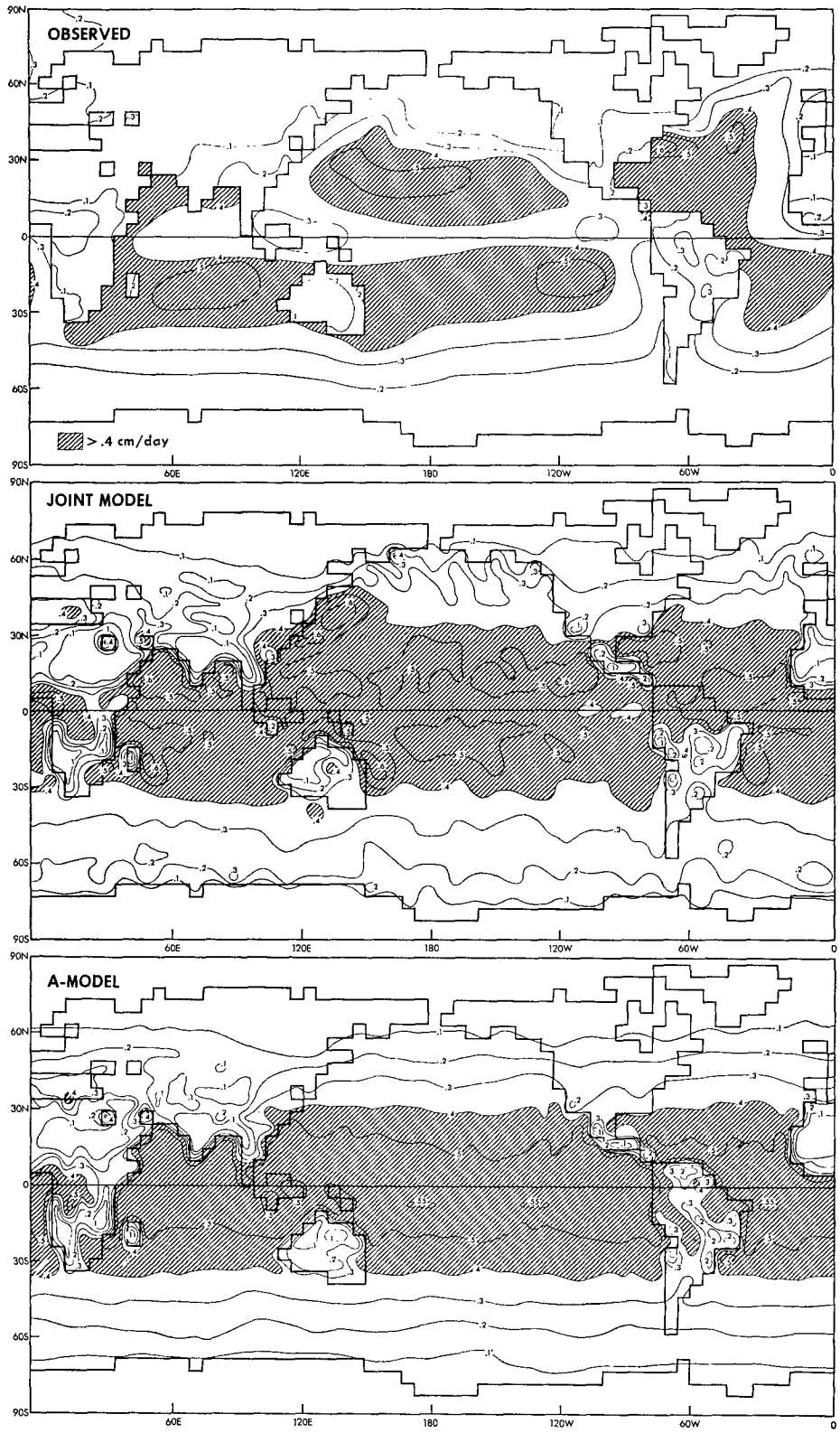

FIG. 15. Global distributions of evaporation rate (cm day^{-1}). Top: observed (estimated by Budyko, 1963); middle: joint model; bottom: A-model.

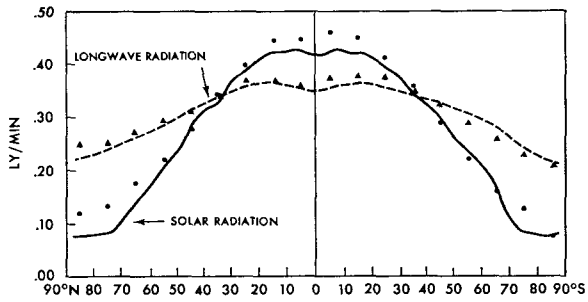

FIG. 16. Latitudinal distribution of radiative fluxes at the top of the atmosphere: net downward solar radiation (solid line, the joint model; ●, observed); upward terrestrial radiation (dashed line, the joint model; ▲, observed). The observed values are obtained by Vonder Haar and Suomi (1971).

Fig. 17 shows the latitudinal distributions for each of the above fluxes for the joint model. Also shown are the observed annual mean values estimated by Budyko (1963). Positive (negative) values indicate heat gain (loss) at the surface. Overall, the agreement of the computed fluxes with Budyko's values is reasonably good. A significant discrepancy exists, however, in the oceanic heat flux in the joint model compared to the observed estimates. Around the equator, the magnitude of negative oceanic heat flux is too weak and the evaporation from the earth's surface is too large. These results are consistent with the warmer-than-observed sea surface temperatures in the equatorial region predicted by the joint model, which was discussed previously. In the Southern Hemisphere, the oceanic heat flux has large positive values around 70S and is much larger than the flux estimated by Budyko. As discussed in Section 4a and in Part II, the supply of heat from lower latitudes to the coastal region of the Antarctic Continent is too large due to the lack of intense surface westerlies in middle latitudes and is responsible for this discrepancy.

In Fig. 18, the horizontal distribution of the oceanic heat flux of the joint model is compared with the actual distribution estimated by Budyko (1963). In middle and high latitudes of the Northern Hemisphere, the oceanic heat flux is very large in the western and northern part of both the Pacific and the Atlantic Oceans in qualitative agreement with Budyko's distribution. Along the eastern boundary of the oceans in the subtropical latitudes, the oceanic flux has large negative values in Budyko's distribution. However, it is small in the joint model. For example, the oceanic flux of the model has small negative values along the west coast of Africa and South America but has small positive or negative values along the west coast of the North American Continent. It is probable that the discrepancy between the observed and the computed results is partly due to the failure of the joint model to simulate quantitatively the intensity of subtropical highs and accordingly the intensity of induced upwelling in the eastern boundary of the oceans.

Along the equator of the joint model, the oceanic heat flux is usually negative and is relatively large in

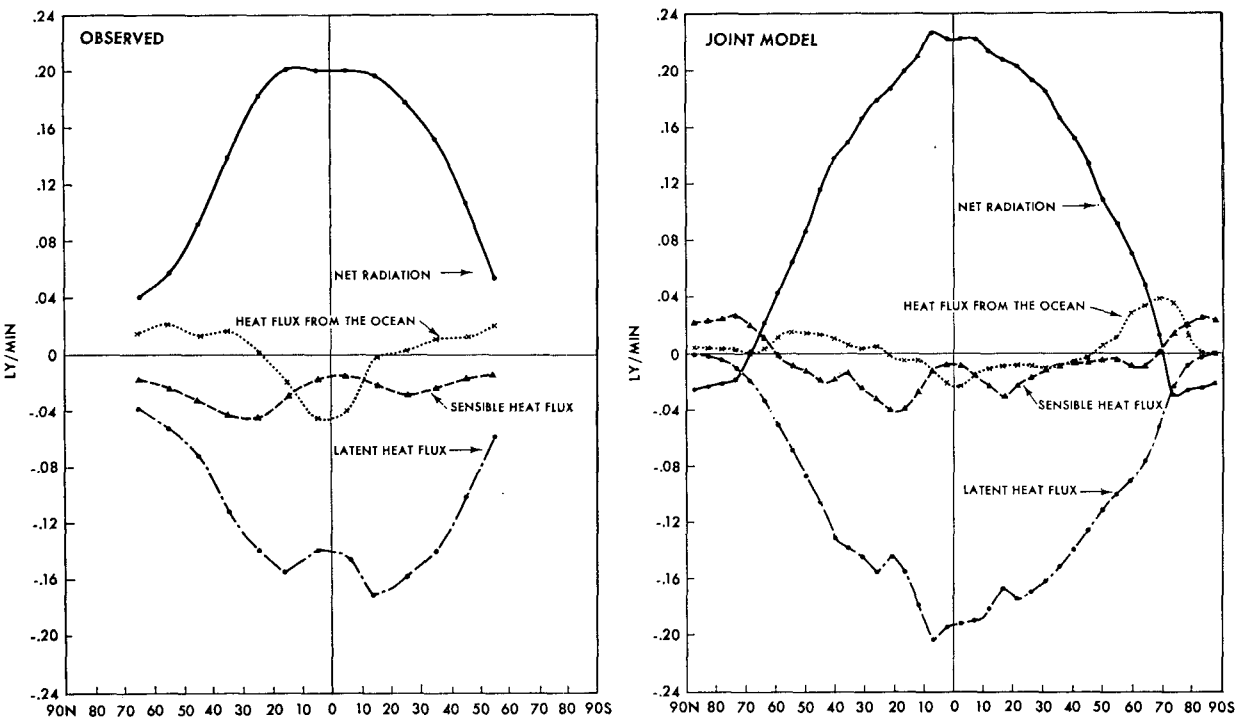

FIG. 17. Latitudinal distributions of the zonal mean values of the heat balance components at the earth's surface (ly min^{-1}). Left: observed (estimated by Budyko, 1963); right: joint model.

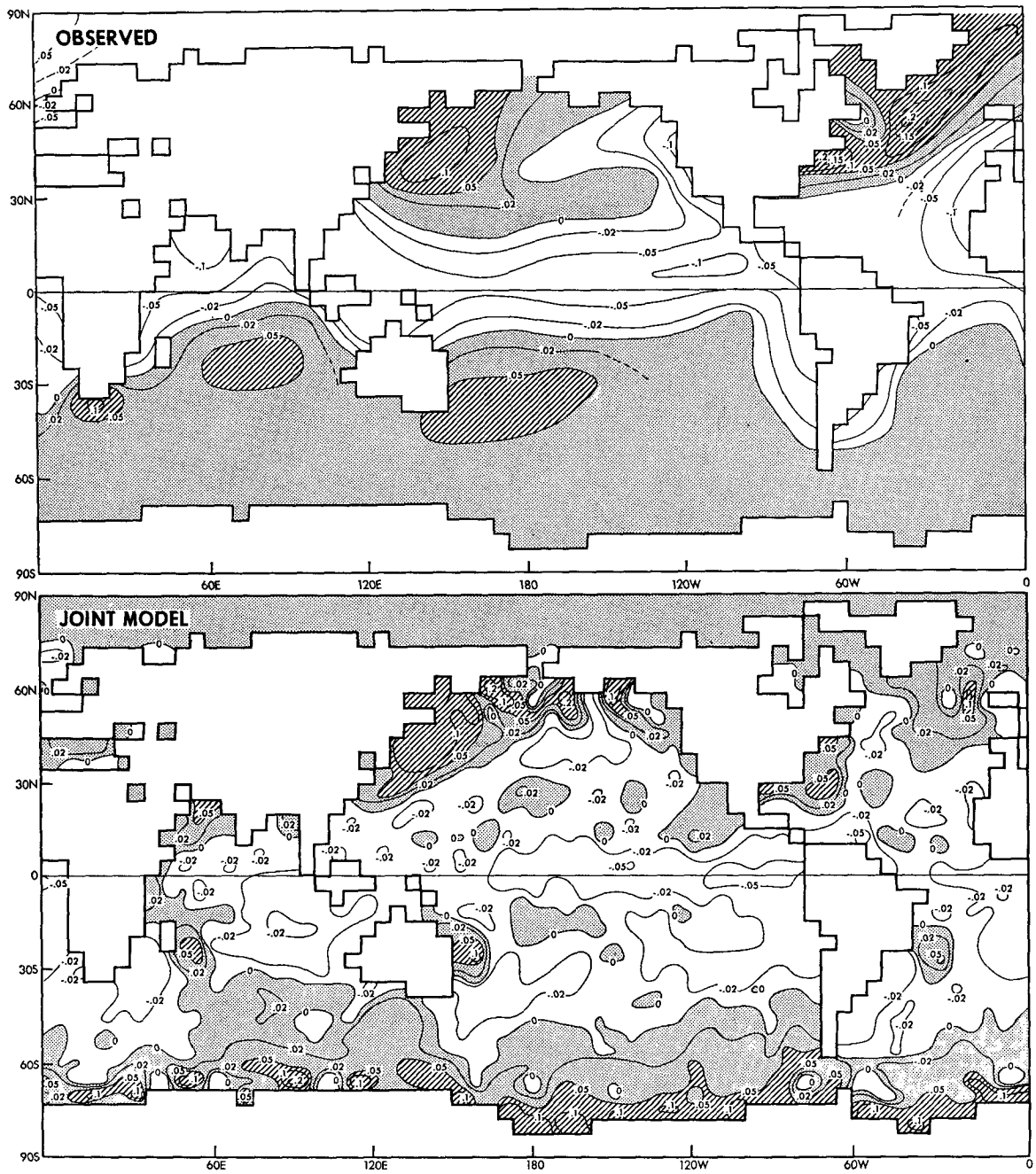

FIG. 18. Horizontal distribution of heat flux (ly min^{-1}) from the interior to the surface of the ocean. Top: observed (estimated by Budyko, 1963); bottom: joint model.

the eastern Pacific. However, its magnitude is not large enough as compared with Budyko's result. In the Southern Hemisphere of the joint model, the oceanic heat flux is unrealistically large along the periphery of the Antarctic Continent as discussed above.

The distribution of oceanic heat flux in Fig. 18 may be compared with Fig. 8, which shows the distribution of the difference between the surface air temperature of the joint model and that of the A-model. As one might expect, regions of positive (negative) oceanic flux generally correspond to regions of positive (negative) temperature difference. However, there are some exceptions. For example, the temperature of the South China Sea increases due to the effects of ocean currents even though the oceanic heat flux has small negative values. In the northwestern Atlantic, the surface air temperatures are lower in the joint model despite the fact that heat flux is positive there. The modification of the

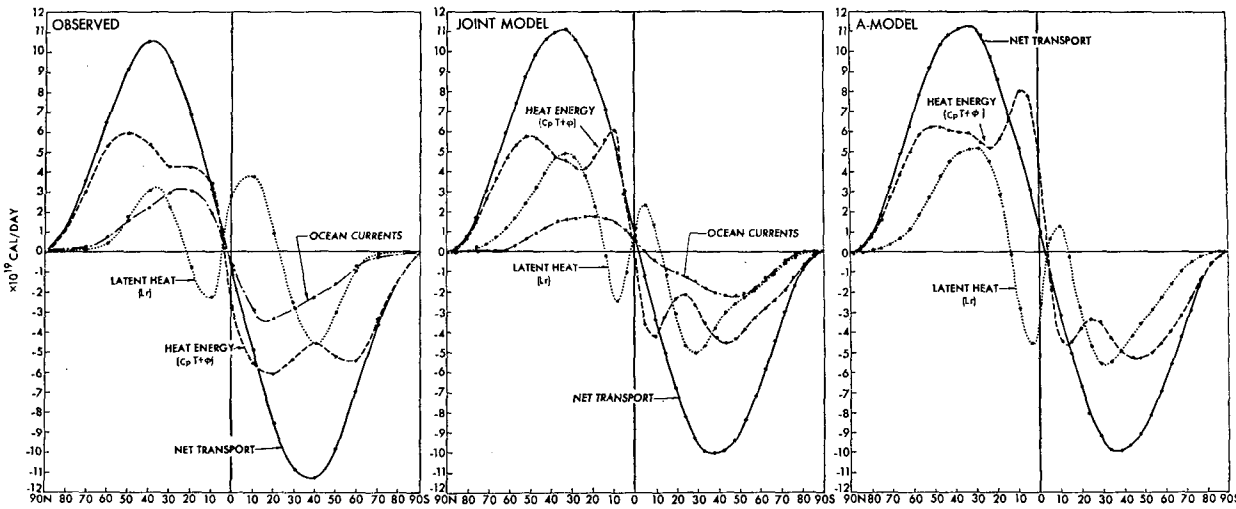

FIG. 19. Latitudinal distributions of the northward transport of energy (10^{19} cal day^{-1}). Left: observed (compiled by Sellers, 1965, following Budyko, 1963); middle: joint model; right: A-model.

direction and the intensity of surface air flow due to the oceanic heat flux significantly alters the air-sea temperature difference and is responsible for these exceptions.

3) MERIDIONAL TRANSPORT OF ENERGY

Meridional transport of energy in the joint ocean-atmosphere system compensates for the radiative imbalance between net downward solar radiation and net upward longwave radiation at the top of the atmosphere. This energy transport occurs by three processes: (i) atmospheric transport of heat energy, i.e., the sum of enthalpy $[c_pT]$, potential energy $[\phi]$ and kinetic energy $[K]$; (ii) atmospheric transport of latent energy $[Lr]$; and (iii) heat transport by ocean currents.

Fig. 19 shows the latitudinal distribution of the energy transport components. Observed data are from Sellers (1965). Positive values represent northward energy transport, while southward transports are negative. In the A-model, net poleward energy transport occurs by the combined processes (i) and (ii) above, whereas in the joint ocean-atmosphere system all three processes contribute to the net transport. In comparing the results of the joint model with the A-model in Fig. 19, we see that the additional heat transport by the oceans in the joint system does not increase the net energy transport. Rather, the amount of energy transport by the joint model atmosphere is reduced, compared to the A-model, so that the net transport remains essentially unchanged. Since the poleward heat transport by ocean currents reduces the meridional temperature gradient and the amplitudes of the baroclinic waves in the atmosphere, it is reasonable that the atmospheric heat transport of the joint model is less than that of the A-model. As discussed in Section 4a, the thermal effect of ocean currents is largest in the lower troposphere and is very small in the upper troposphere. Therefore, the net outgoing radiation at the top of the atmosphere is affected little by the oceanic heat transport.[6] This is why the total poleward transport of energy required from the overall radiation imbalance is hardly affected by the ocean circulation.

Fig. 19 also indicates that the latitudinal distribution of the total poleward transport by the ocean-atmosphere system of the joint model agrees reasonably well with the estimate of the actual transport. This agreement is consistent with the earlier finding that the latitudinal distribution of the net radiation flux at the top of the atmosphere is not very different from the estimate of this quantity for the actual atmosphere (see Fig. 16).

The magnitude of the heat transport in the joint model ocean falls short of the observed estimate. In the Northern Hemisphere, the transport is at a maximum around 20N in qualitative agreement with the Seller's distribution. However, the maximum transport occurs around 50S in the Southern Hemisphere and does not agree with the estimate of the actual transport shown in the left side of Fig. 19. For further discussion of the oceanic heat transport, see Section 7 of Part II.

5. Concluding remarks

The global ocean-atmosphere model, which is described in this study, simulates some of the basic features of the climate. However, it has many shortcomings. For example, the belt of large gradient of sea level pressure in middle latitudes of the Southern Hemisphere is missing in the joint model atmosphere. Also the intensities of the subtropical highs are significantly underestimated by the model. The latter shortcoming

[6] The fluxes of radiation at the top of the A-model atmosphere are not shown in Fig. 16 because they differ little from those of the joint model shown in this figure.

is responsible for the unsatisfactory simulation of arid regions such as the Sahara, Australian desert, and trade wind regions. Holloway and Manabe (1971) have shown that increasing the computational resolution of horizontal finite differencing results in the increase of baroclinic activity in middle latitudes and the intensification of the subtropical highs in the model (see also Manabe *et al.*, 1970). It is therefore probable that at least this difficulty of the present model can be eliminated by increasing the computational resolution of the model.

Despite the various limitations of the model mentioned above, it is possible to identify some of the effects of ocean currents upon the climate by comparing the results from the joint model with those from the A-model, in which the effects of ocean currents are absent.

In general, the poleward transport of heat by ocean currents results in the cooling of the atmosphere in low latitudes and heating in high latitudes. The magnitude of the cooling near the surface is much smaller than that of the heating because, in low latitudes, the thermal effect of ocean currents spreads throughout the troposphere, whereas in higher latitudes, it is limited to the lower troposphere by stable stratification. Furthermore, the warming effect by ocean currents is magnified in the subarctic region because of snowmelt and the resulting decrease of surface albedo.

It is interesting that the total poleward transport of energy by the joint ocean-atmosphere system is affected little by the effects of ocean currents. In other words, the oceanic contribution is compensated by a decrease in the atmospheric transport resulting from the reduction in meridional temperature gradient in the lower troposphere. Since the temperature change due to the effect of ocean currents is small in the upper troposphere and the stratosphere, the net upward radiation at the top of the atmosphere is hardly changed by this effect. Therefore, the total poleward transport of energy required from the radiative imbalance is hardly altered.

According to the comparison between the sea level pressure of the joint model with that of the A-model, both the Aleutian low and the Icelandic low shift poleward and intensify due to the increase in land-sea contrast in surface temperature resulting from the heat transport by ocean currents. On the other hand, the subtropical anticyclones over the oceans weaken because of the general reduction of baroclinicity in middle latitudes.

The oceanic heat transport is responsible for raising the surface temperature in the northeastern boundary of both the Pacific and the Atlantic Oceans. The northward heat transport by the subarctic gyre is partly responsible for this warming. Furthermore, the northward shift and the intensification of the Aleutian low mentioned above increase the southerlies. Accordingly, the advection of warm air over the northwestern part of North American Continent raises the surface temperature there. The melting of snow cover tends to amplify this warming by markedly reducing the surface albedo. On the other hand, the surface air temperature in the northeastern part of the Eurasian Continent of the joint model is lower than the corresponding temperature of the A-model. The northward shift and the intensification of the Aleutian low increase the southward advection of cold air in this region and cause this cooling. Over the Kuroshio current and Gulf Stream the surface temperature increases significantly due to the advection of warm water by the subtropical gyre. The rate of precipitation also increases somewhat in those regions. Over the equator and along the west coast of continents in the subtropics, the upwelling of cold water lowers the sea surface temperature and causes a significant decrease of precipitation. The equatorial upwelling reduces the mass transport in the upward motion branch of the Hadley cells. In general, the rate of precipitation tends to increase where the temperature of the ocean surface increases significantly by the effects of ocean currents and decreases in the areas of surface cooling.

There are many differences between the climates from the two models in the Southern Hemisphere. For example, the sea surface temperature of the joint model is much warmer than that of the A-model along the periphery of the Antarctic Continent. However, it is doubtful that these differences represent the actual effects of ocean currents in view of the inability of the models to simulate satisfactorily the distributions of sea level pressure and surface temperature in the high latitude region of the Southern Hemisphere.

One of the main objectives of the present study is to perform a test of the preliminary version of the joint ocean-atmosphere GFDL model. In view of the many shortcomings of the model, the conclusions obtained from this study should be regarded as tentative. It is encouraging, however, that the model climate resembles the actual climate to a certain degree. Further increase of the resolution of horizontal finite differencing seems to be required for a better simulation of climate. We plan to continue the time integration after halving the grid size. As suspected already, some of the failures of the model to reproduce the features of the actual climate may stem from the lack of seasonal variation of solar radiation. A joint ocean-atmosphere model with seasonal variation is being tested at the present time.

Acknowledgments. The authors gratefully acknowledge the assistance of J. Leith Holloway, Jr., for developing the economical scheme of Fourier filtering used in the model, and Ronald Pacanowski for monitoring the computations in the oceanic part of the monitoring the computations in the oceanic part of the joint model. We wish to express our appreciation to Dr. J. Smagorinsky for his constant encouragement and

valuable support so vital to a project of this nature. We are indebted to the members of the GFDL staff who assisted with the preparation of the manuscript and figures, and in particular to Elaine D'Amico, Edwin Green and Philip Tunison.

APPENDIX

Derivation of the Smoothed Topography

The topography of the earth's surface used in both the joint model and the A-model is shown in Fig. 3. The basic data for the terrain elevations are taken from Scripps Institute of Oceanography data (Smith *et al.*, 1966). The Scripps data are interpolated to the latitude-longitude grid and smoothed by use of the function

$$\bar{z}=0.25z_0+\sum_{i=1}^{8}(w_i z_i),$$

where z_0 is the unsmoothed height at the central grid point, z_i the height at the surrounding grid point i, w_i a weighting factor (normalized so as to make the sum of the weights equal to 0.75), and $\bar{z}$ the resulting smoothed height. The summation is over the eight surrounding contiguous boxes in the grid.

The Scripps data contain ocean-bottom topography as negative values in addition to positive land-height values. All data are used, and when a negative smoothed height occurs at a grid point which had been above sea level in the input data, the original shoreline is restored (i.e., the height is redefined as +1 m). Mathematical eroding of the coasts is reduced by halving the ocean depths before smoothing the combined land and ocean-bottom topography.

In addition to the space smoothing mentioned above, it is necessary to apply the Fourier space filter to the surface topography at the beginning of the time integration. This filter is applied only at higher latitudes, in the same manner as for the prognostic variables. Refer to Section 2b for details of the Fourier filter.

REFERENCES

Bjerknes, J., L. J. Allison, E. R. Kreins, F. A. Godshall and G. Warnecke, 1969: Satellite mapping of the Pacific tropical cloudiness. *Bull. Amer. Meteor. Soc.*, **50**, 313–322.

Bryan, K., 1966: A scheme for numerical integration of the equations of motion on an irregular grid free of nonlinear instability. *Mon. Wea. Rev.*, **94**, 39–40.

——, 1969: Climate and the ocean circulation: III. The ocean model. *Mon. Wea. Rev.*, **97**, 806–827.

——, S. Manabe and R. C. Pacanowski, 1975: A global ocean-atmosphere climate model. Part II. The oceanic circulation. *J. Phys. Oceanogr.*, **5**, 30–46.

Budyko, M. I., 1956: *Heat Balance of the Earth's Surface.* Leningrad, Gidrometeor, 254 pp.

——, 1963: *Guide to the Atlas of the Heat Balance of the Earth.* Moscow, Gidrometeoizdat, 69 pp.

Crutcher, H. L., and J. M. Meserve, 1970: Selected level heights, temperatures, and dew points for the Northern Hemisphere. NAVAIR 50-1C-52, U. S. Naval Weather Service, Washington, D. C.

Grimmer, M., and D. B. Shaw, 1967: Energy-preserving integrations of the primitive equations of the sphere. *Quart. J. Roy. Meteor. Soc.*, **93**, 337–349.

Hering, W. S., and T. R. Borden, Jr., 1965: Mean distributions of ozone density over North America, 1963–1964. Environmental Res. Papers, No. 162, AFCRL, 19 pp.

Holloway, J. L., Jr., and S. Manabe, 1971: Simulation of climate by a global general circulation model. *Mon. Wea. Rev.*, **99**, 335–370.

——, M. J. Spelman and S. Manabe, 1973: Latitude-longitude grid suitable for numerical time integration of a global atmospheric model. *Mon. Wea. Rev.*, **101**, 69–78.

Kung, E. C., R. A. Bryson and D. H. Lenschow, 1964: Study of a continental surface albedo on the basis of flight measurements and structure of the earth's surface cover over North America. *Mon. Wea. Rev.*, **92**, 543–564.

Kurihara, Y., and J. L. Holloway, Jr., 1967: Numerical integration of a nine-level global primitive equations model formulated by the box method. *Mon. Wea. Rev.*, **95**, 509–530.

Leith, C., 1969: Numerical simulation of turbulent flow. *Properties of Matter under Unusual Conditions*, H. Mark and S. Fernback, Eds., Interscience, 267–271.

——, 1973: The standard error of time-average estimates of climate means. *J. Appl. Meteor.*, **12**, 1066–1069.

London, J., 1957: A study of the atmospheric heat balance. Final Report, Contract AF19(122)-165, Dept. Meteor. Oceanogr., New York University, 99 pp.

——, 1962: Mesosphere dynamics: Part III. The distribution of total ozone in the Northern Hemisphere. Final Report, Contract AF19(604)-5492, Dept. Meteor. Oceanogr., New York University, 68-108.

Lvovitch, M. I., and S. P. Ovtchinnikov, 1964: River drainage. *Physical-Geographical Atlas of the World.* Academy of Sciences USSR and Central Administration of Geodesy and Cartography of the USSR, Moscow, 60–61.

Manabe, S., 1969a: Climate and the ocean circulation: I. The atmospheric circulation and the hydrology of the earth's surface. *Mon. Wea. Rev.*, **97**, 739–774.

——, 1969b: Climate and the ocean circulation: II. The atmospheric circulation and the effect of heat transfer by ocean currents. *Mon. Wea. Rev.*, **97**, 775–805.

——, and R. F. Strickler, 1964: Thermal equilibrium of the atmosphere with a convective adjustment. *J. Atmos. Sci.*, **21**, 361–385.

——, J. Smagorinsky and R. F. Strickler, 1965: Simulated climatology of a general circulation model with a hydrologic cycle. *Mon. Wea. Rev.*, **93**, 769–798.

——, and R. T. Wetherald, 1967: Thermal equilibrium of the atmosphere with a given distribution of relative humidity. *J. Atmos. Sci.*, **24**, 241–259.

——, and K. Bryan, 1969: Climate calculations with a combined ocean-atmosphere model. *J. Atmos. Sci.*, **26**, 786–789.

——, J. Smagorinsky and H. M. Stone, 1970: Simulated climatology of a general circulation model with a hydrologic cycle. *Mon. Wea. Rev.*, **98**, 175–212.

——, D. G. Hahn and J. L. Holloway, Jr., 1974: The seasonal variation of the tropical circulation as simulated by a global model of the atmosphere. *J. Atmos. Sci.*, **31**, 43–83.

Matsuno, T., 1966: Numerical integration of primitive equations by use of a simulated backward difference method. *J. Meteor. Soc. Japan*, **44**, 76–84.

Minitz, Y., 1965: Very long-term global integration of the primitive equations of atmospheric motion. WMO Tech. Note No. 66, 141–167.

Penn, S., 1957: The prediction of snow vs. rain. Forecasting Guide No. 2, U. S. Weather Bureau, Washington, D. C., 29 pp.

Phillips, N., 1957: A coordinate system having some special advantages for numerical forecasting. *J. Meteor.*, **14**, 184–185.

Posey, J. W., and P. F. Clapp, 1964: Global distribution of normal surface albedo. *Geofis. Intern.*, **4**, No. 1, 33–48.

Sellers, W., 1965: *Physical Climatology*. The University of Chicago Press, 272 pp.

Smagorinsky, J., 1963: General circulation experiments with the primitive equations: I. The basic experiment. *Mon. Wea. Rev.*, **91**, 99–164.

——, S. Manabe and J. L. Holloway, Jr., 1965: Numerical results from a nine-level general circulation model of the atmosphere. *Mon. Wea. Rev.*, **93**, 727–768.

Smith, S. M., H. W. Menard and G. F. Sharman, 1966: Worldwide ocean depths and continental elevations averaged for areas approximating one degree squares of latitude and longitude. SIO Ref. Rept. 65-8, Scripps Institute of Oceanography, 14 pp.

Taljaard, J. J., H. van Loon, H. L. Crutcher and R. L. Jenne, 1969: *Climate of the Upper Air, Part I. Southern Hemisphere, Vol. 1, Temperatures, Dew Points, and Heights at Selected Pressure Levels*. NAVAIR 50-1C-55, U. S. Naval Weather Service, Washington, D. C.

Vanderman, L., 1970: Global forecasts on a latitude-longitude grid with primitive equation models. *Proc. Intern. Seminar of Tropical Meteorology*, Campinas, S. P., Brazil, 25 September–10 October, 1969, Escritorio de Meteorologia (M.A.), Brasilia, 233–269.

Vonder Haar, T. H., and V. Suomi, 1971: Measurements of the earth's radiation budget from satellites during a five-year period. Part I: Extended time and space means. *J. Atmos. Sci.*, **28**, 305–314.

Wetherald, R. T., and S. Manabe, 1972: Response of the joint ocean-atmosphere model to the seasonal variation of the solar radiation. *Mon. Wea. Rev.*, **100**, 42–59.

Yamamoto, G., 1952: On a radiation chart. *Sci. Rept. Tohoku Univ., Geophys. . Ser.*, **4**, No. 1, 9–23.